NASA Contractor Report 166017

DEVELOPMENT OF CLOSED LOOP ROLL CONTROL FOR MAGNETIC BALANCE SYSTEMS

Eugene E. Covert, Charles W. Haldeman,
Gautham Ramohalli, and Peter Way

MASSACHUSETTS INSTITUTE OF TECHNOLOGY
Cambridge, Massachusetts 02139

Grant NSG-1502
October 1982

National Aeronautics and
Space Administration

Langley Research Center
Hampton, Virginia 23665

PREFACE

This Final Report covers work performed on NASA Grant NSG-1502 between 1 February 1978 and 31 January 1982 under the Technical Cognizance of Mr. Richmond P. Boyden, Transonic Aerodynamics Division, NASA Langley Research Center.

The use of trade names in this paper is essential to a proper understanding of the subject material; their use in no way constitutes official endorsement, either expressed or implied, by the National Aeronautics and Space Administration.

Page Missing in Original Document

TABLE OF CONTENTS

CHAPTER 1

INTRODUCTION

Magnetic model suspension and balance systems for wind tunnel use (1) have been designed, tested and used at MIT's Aerophysics Laboratory for over eighteen years. These research programs which have been funded by the USAF, NASA, Army Ballistics Research Laboratory and the Army Research Office among others have led us to explore the many unique capabilities of the magnetic balance for aerodynamic testing. Among these are the precise measurement of forces (2,3,4), the measurement of wakes behind cones (5,6), spinning bodies at angle of attack (7), as well as forces and moments on spinning bodies (9) and studies of ring airfoils (10), and the production of forced simultaneous spinning and coning model motion in the subsonic flow (11).

Since the original studies of the roll control problem for symmetric magnetic suspension by Stephens (12,13) who described possible methods for extending control to the roll degree of freedom, only forced roll rate had been produced on a consistent basis (7,9,10,11) before the present research grant. This research was undertaken with the goal of demonstrating closed loop control of the roll degree of freedom on the NASA prototype magnetic balance at the MIT Aerophysics Laboratory, thus showing feasibility for a roll control system for any large magnetic balance system which might be built in the future. During the research under this grant, study was directed toward the several areas of torque generation, position sensing, model construction and control system design. These efforts were then integrated to produce successful closed loop operation of the analogue roll control system. This experience indicated the desirability of microprocessor control for the angular degrees of freedom and work was started in this direction. This

phase of the work, however, could not be completed within the available budget, so work was stopped. Each of the three parts, roll position sensing, production of roll torque and stabilization of the feedback loop will be discussed in detail below.

CHAPTER 2

GENERATION OF ROLLING MOMENT

Production of rolling moment in magnetic balance systems has been investigated by Stephens (12,13). He suggested three possible methods:

a. Interaction between transverse D.C. field components and a transverse or nonsymmetrical model magnetization. While this method appears to have the greatest torque-producing capability, the presence of the full matrix of magnetization and applied field components with the resulting complicated interactions requires a full digital magnetic balance control system (14) to provide data reduction and model control with acceptable effort and accuracy. Model construction is also difficult for this case.

b. Interaction between a single phase transverse A.C. field of controlled transverse angle with a model supporting a conducting plane or loop which can be located inside the wing area. This method has the advantage of producing reasonable torque at low roll rates and is independent of the lift, slip, and drag degrees of freedom. This method was used in initial roll experiments (12).

c. Interaction between a rotating two-phase transverse A.C. field and a copper plated or other conducting model. This method has been used for some time (9,15) to produce high roll rates for magnus testing with the NASA prototype balance, and more recently with spinning and coning models (16). This method produces higher roll rates than method b, but lower torques. It will, of course, also work with the loop described in (b). This method is independent of all other degrees of freedom.

Because of the need for relatively large rolling moments for testing winged bodies, and the need to use existing balance coils, research reported

with the roll system concentrated on method b. A qualitative model of the torque generation process is discussed below.

Torque on Circular Loop

Consider a circular loop of wire of radius a, as shown in Figure 1. Here an A.C. magnetic field of angular frequency ω and amplitude B_o intersects the plane of the loop at an angle θ. The resultant field near the loop is the sum of the applied field B_o and the induced field B produced by the current circulating in the ring. The field of this current has been given by Stratton (17). In the plane of the wire loop the field is purely axial and Stratton's expression reduces to

$$H_z = \frac{\mu_o I}{2\pi\left(1 + \frac{r}{a}\right)} \; K(k) + \frac{1 - \left(\frac{r}{a}\right)^2}{\left(1 - \frac{r}{a}\right)^2} \; E(k)$$

where K and E are the complete elliptic integrals of argument

$$k^2 = \frac{4\frac{r}{a}}{\left(1 + \frac{r}{a}\right)^2}$$

A plot of the field distribution is shown in Figure 2, using tabulated values of K and E (18). Here solid points and the solid line show the field of the wire loop alone. When this loop current is generated by an applied uniform field, $B_o \sin \omega t$, the current will build up to a level such that the area A equals the area B, leaving zero net flux linking the loop if it has zero resistance.

If the loop has finite resistance, area B will be greater than area A by a sufficient amount to provide EMF to drive the ring current. Since $\int$ Eds about the loop = $(d/dt)(\int B \cdot dA)$ over a loop area, the difference between areas B and A (uncancelled driving flux) will decrease as frequency

is increased. There will also be a phase difference between the applied field and the induced field. It is these effects as well as the complex geometry of actual models which makes detailed calibrations necessary. When the applied field B_o makes an angle θ to the plane of the ring, only the perpendicular component B is cancelled by the induced current, where

$B = B_o \sin \omega \sin \theta$.

The force on the wire acting normal to the plane of the loop produces rolling moment. This force is proportional to the current I and the parallel field component $B_o \sin \omega t \cos \theta$. The torque (rolling moment) acting on the loop is found by integrating around the wire loop, resulting in

$$\tau = c\, a^2 B_o^2 \sin 2\theta (1 - \cos 2\omega t) \qquad (1)$$

where c is a constant that depends on loop geometry resistance and frequency. As was expected the rolling moment peaks at $\theta = 45°$ and has both average and periodic components. From measurements of the torque on a copper ellipse of 6.35 cm semi-major axis, 2.22 cm semi-minor axis and 0.3 cm thick in the 400 Hz magnetic balance field, the constant c was found to be approximately 0.26 dyne-cm/cm^2 gauss^2 (19).

The circuit used to apply variable amplitude 400 Hz power (or quadrature 1200 Hz power) to the pitch and yaw coils is shown in Figures 3 and 4. Here the D.C. is isolated from the roll amplifiers by series capacitors and parallel L-C traps are used for isolation of the 20 KH_Z position sensing signals and 400 Hz (1200 Hz) roll power. Methods for developing the control signals for the roll power supplies are discussed later in this report.

CHAPTER 3

POSITION SENSING

Many methods of remotely sensing model position within a magnetic balance have been used. The electromagnetic position sensor (EPS) employed with the MIT-NASA balance has been one of the most successful because it presents the following advantages:

a. Five components of model position have previously been derived very accurately over a large range without first order coupling. For control purposes the signals are adequate to stabilize a model over the entire cross section of the test section.

b. This method is not sensitive to perturbations within the test section such as smoke, pressure probes and balance operators.

c. The EPS can be made to be insensitive to model geometry. Frequently, different models can be suspended without retuning any of the control equipment. Changing from ferromagnetic to copper plated models requires a simple adjustment of the demodulators.

Since the ferromagnetic cores used with the magnetic balance until now have been symmetric about the wind axis, roll information has not been detectable by the EPS. Indeed, such symmetry is desirable. From a functional standpoint one should extend the capabilities of the EPS to the measurement of roll angles. In this section an experimental method of developing roll signals with the existing EPS coils is presented with a description of the required circuitry.

Although the operation of the EPS system has been reported in detail by Stephens (13) for the five degree of freedom case, it is instructive for the purpose of developing the roll position sensor (RPS) to describe this system from a different perspective.

The EPS coil arrangement is shown schematically in Figure 5 with a sectional view in Figure 6 and the connection schematic in Figure 7 from Stephens (13). The system consists of a pair of Litz-wire wound Helmholtz excitation coils and 14 pick-up coils arranged as shown on the surface of a cylinder. The coil parameters are given in Table 1. A detailed mathematical analysis of this process is given in Appendix A. The EPS is centered at the magnetic center of the balance. The excitation coils are driven at 20 KHz by a high stability audio-oscillator and power-amplifier combination. They produce a highly uniform axial field within the test section. The pick-up coils consist of 30 turns of No. 30 teflon-coated wire arranged to be orthogonal to the desired component of the excitation field. Each coil is connected to the one directly across the test section and in the same sense; for example, a D.C. current applied to the H2A-H2B combination in Figure 5 would produce an additive field along the y axis. The notable exception to this rule is the drag coil pair marked AX in Figure 5. This pair is coaxial with the Helmholtz coils and connected in opposition. Since the coils are arranged to link no net flux without a model perturbation, no voltage should be developed in the EPS when a model is not present. In practice, small residual couplings between coils exist. These are nulled in the demodulation circuitry.

When a ferromagnetic model or a diamagnetic model is placed within a uniform oscillating field, the field is perturbed (Appendix A). A diamagnetic model can be constructed by copper plating a ferrous model to a depth greater than the effective skin depth of the conductor at the frequency of interest. The applied field then "sees" only the copper, because currents flow in the

---

* Litzendraht conductor, which is called "Litz-wire," is a cable of many fine insulated wires that is twisted in its manufacture such that the resultant cable has low resistance to both direct and to alternating current.

Table 1

NASA Prototype Balance
EPS Coil Parameters

EPS Coil Circuit	DC Resistance[1] ohms	Inductance[2] millihenrys	Self-capacitance[3] microfarads
Axial	14.76	.919	.00141
Lateral I	7.57	.468	.00156
Lateral II	10.41	.517	.00143
Lateral III	7.18	.416	.00126
Vertical I	12.42	.509	.00144
Vertical II	9.49	.502	.00146
Vertical III	12.47	.488	.00152

(1) Measured with Fluke digital VOM.

(2) Calculated from resonance frequency with .25 μf mica transmitting capacitor.

(3) Calculated from self-resonant frequency.

conductor, which exclude the changing field. Thus the effect of a diamagnetic model is to cancel a portion of the applied field.

The practical effect of the copper plate is to remove coupling which would otherwise exist between the DC support fields and AC position sensing fields. When a ferromagnetic ellipsoid is placed within a uniform field, the magnetization within the volume is constant and adds to the applied field. If the ellipsoid is diamagnetic, μ is negative and the magnetization opposes the applied field. The resultant field is the sum of the dipole field due to magnetization of the model and the applied field. For the purpose of discussion it will be assumed that the field builds up in phase with the applied field for both the ferromagnetic and diamagnetic cases, although in practice the magnetization or induced field will be slightly phase shifted due to ohmic losses in the model. The field due to the model is also assumed to be tied to the model and to rotate with it for small angles. It is this effect which is exploited to detect roll position.

For the axisymmetric case the process of detection has been described by Stephens (13). It is desirable to convert the AC voltage at the pick-up coils to a DC voltage proportional to model position. This can be done ideally by multiplying the pick-up coil voltage by a reference in phase with it and then averaging over a period. Consider now just a pair of field lines issuing from the model at a particular time t. The applied field and the model are shown in Figure 8. If the model is centered, the voltage induced in all the coils is zero. Here the model is moved in drag, lift and pitch. The letters next to the lines of flux indicate the voltage developed in each coil due to the component of flux perpendicular to their surface. The convention here is that H_x is expanding and the area vector is positive radially outward. Only the V1, V2, V3 and drag coils are shown here; the results apply equally well to yaw and slip by symmetry. The total voltages developed in each coil are given for each configuration.

From these diagrams it follows that to first order pure drag signals are measured by AX without lift or pitch coupling. Lift can be measured from V1-V3 and pitch is given by V1 + V2 + V3. It is interesting to note that V2 contributes nothing to linear model motions. A general statement about position sensing in this manner is that linear motions are detected by subtracting coil outputs and rotations are detected by summing coil outputs. Similar drawings can be made to show that the coils are only sensitive to motions perpendicular to their surface.

Roll Loop

The roll position can only be detected by the EPS coils if the model has some magnetic asymmetry about its equatorial plane. To this end an elliptical copper loop has been fastened to it at some small angle of incidence, as in Figure 9. If a perfectly conducting loop is considered by itself and a field is generated in it to exactly counteract the component of B_x perpendicular to it, the RMS radial component of field is then

$$B_r = \frac{B_x}{2} \sin 2\theta \qquad (2)$$

The end view in Figure 10 shows the effect of the loop alone on the pick-up coils as the roll angle changes. Since all the transverse flux leaving the EPS reenters it, voltages are developed in each coil due to each flux line as described before. The pitch and yaw signals from the V and H coils now contain a roll component. These components are found experimentally to be proportional to the sine and cosine of roll angle ϕ.

When the loop is placed around a ferromagnetic model at a small angle of incidence, several changes take place in the far field measured by the EPS. A relatively strong AC transverse field now exists which magnetizes the model along its short axis. While the field due to the model alone

rotates with it in roll, equation (1) implies that the transverse field due to the loop varies as twice the pitch angle, thus producing coupling between pitch, yaw and roll. Since the model perturbation field has a different phase for diamagnetic and ferromagnetic materials, the pitch and yaw coil signals contain a quadrature component which depends on roll angle. These can be demodulated separately to give signals proportional to pitch, yaw and roll. In the prototype roll position sensor RPS, the nature of the coupling was assumed to be linear and attempts were made to null this effect by crossfeeding, pitch, yaw and roll. This method was only effective for small roll angles (about ± 30 degrees about the set point).

Position Signal Demodulation

The signals received at the pick-up coils are sinusoidal and amplitude modulated. Stephens (13) has described a method of demodulation and the associated electronics. In order to obtain roll information as well as true pitch and yaw, a roll position sensor was devised. It takes the AC pitch and yaw signals from the five degree of freedom system after they are combined and demodulates them with respect to separate references. Figure 11 is a block diagram of the roll position sensor (RPS). A suitably phased reference is formed by adding in phase and quadrature signals. The incoming pitch or yaw signals are multiplied by each reference and then low pass filtered to obtain an average value. The output stage contains a mixing circuit which can be used to decouple pitch and yaw from roll. Two identical channels are required--one for pitch and sin θ and one for yaw and cos θ.

Roll Position Sensor Circuit

The schematic for the RPS is given in Figure 12. Although the function of the circuit is similar to the five degree of freedom EPS system, the components have little resemblance. Considerable effort has been devoted

to reducing the temperature drift and coupling which have caused small position errors in the past. The following areas for improvement were identified:

a. Operational amplifiers in the EPS system have insufficient gains at 20 KHz.--Open loop gain is described by Jung (21) to be the single most important parameter in describing the ultimate accuracy of an operational amplifier. Total harmonic distortion, output resistance and sensitivity to gain variations are each reduced by the factor

$$K = \frac{1}{1 + \beta A} \tag{3}$$

where A is the open loop gain, and β is the voltage attenuation of the feedback network. These concepts are best illustrated by an example. The Nexus operational amplifiers used in the EPS demodulator have an open loop gain of 100 at 20 KHz. If a unity gain inverting stage is chosen, $\beta = 0.5$; therefore, $K = 0.02$. The open loop output impedance is 5000 ohms for this amplifier and is transformed to 100 ohms closed loop. This is a large output impedance for an operational amplifier and successive stages will load it unless their input impedances are very high.

b. The slewing rate of the EPS operational amplifiers is not high enough to follow 20 KHz signals of 10 volt amplitude.--The total output range cannot be utilized and the signal-to-noise ratio is reduced. The slewing rate, SR, required to reproduce a signal of amplitude a is given by

$$SR = a\omega \tag{4}$$

For the case of 20 KHz, 10 volt signals SR must exceed 1.26 V/μS. The Nexus amplifiers in the EPS system only offer a slew rate of 1.1 V/μS.

c. The phase sensitive demodulators used in the EPS system operate only over a small input voltage range before the transformers saturate.-- Furthermore, distortion due to the turn-on transient is observed when the signal amplitude is small.

An effort has been made in the design of the roll position sensor system to eliminate some of the above deficiencies. The high frequency amplifiers are Analog Devices AD518 operational amplifiers. They have open loop gains of 65 db at 20 KHz. For comparison purposes, K = 0.001 for the unity gain inverter. This yields a factor of 20 improvement in gain performance. The 70 V/μS slewing rate of this amplifier allows full utilization of its output range. These amplifiers are very sensitive to capacitive loads, however, and must be suitably isolated. The ring demodulators have been replaced with laser trimmed precision monolithic multipliers. They feature less than 1 percent total error and better linearity than the phase sensitive ring demodulators. In addition, they are capable of operation over the full 20-volt range.

The low pass filter is designed to attenuate the high frequency components of the demodulator output and give a measure of the DC value of the signal. It consists of three stages. The first is a passive low pass filter with two poles at 1000 Hz. The second adds two poles at 100 Hz and the third has a pole at 48 Hz. The DC gain of the total filter is approximately 16 and its attenuation of components above 400 Hz is greater than 44 db. The design of this filter has not yet been optimized. Possible modifications are suggested later.

The mixing circuit on the output gives a method of nulling the coupling between roll and pitch and yaw. It is possible to add up to the full roll output or its inverse to pitch and yaw and vice versa.

To test the output of the roll sensor the model, Figure 9, was supported in a pivoted Lucite cage and rolled about the long axis of the ellipsoid while the outputs of horizontal roll and vertical roll were displayed on an x-y plotter (19). The resulting maps are shown in Figure 13 with pitch angle of the ellipsoid axis, θ, as a parameter. Note that at $\theta=0$ the map is very close to the ideal circle with usable control regions in all quadrants. As θ is increased, however, the symmetry of the output disappears with a region usable for analog control limited to about $\phi = 30°$ to $\phi = 150°$, for $\theta = -5°$ and $-10°$ and $\phi = 210°$ to $\phi = 330°$, for $\theta = +5°$ and $+10°$. This is the effect which limited the operating range of the analog roll system and suggested development of a digital control system using microprocessors.

CHAPTER 4

OPERATION OF THE ROLL SYSTEM

From Eq. (1) it is apparent that a time average rolling moment on the inclined loop can be generated when the applied AC field makes a non-zero angle with the plane of the loop shown in Figure 14. Two possible methods of controlling the total field are:

a. The total field magnitude can be maintained constant and rotated as necessary by the control system. The average torque is found by resolving B into its components, as in Figure 14.

$$T_a = -K_{ac} \frac{|\vec{B}|^2}{4} \sin 2\theta \qquad (5)$$

where θ is the angle between the field vector and the loop plane. The torque constant K_{ac} is defined by comparison with the average of equation (1). When the field is aligned with the plane of the loop, there is no rolling moment since it links no flux.

b. The total field amplitude can be modulated while maintaining the resultant angle at ± 45 degrees to the loop plane. Maximum torque is therefore available for any given applied field strength. This method was tried first because there is a relatively straightforward means of developing the roll drive signals for a full rotation of the model. This method makes calculating torque from current simpler since θ need not be determined at each data point.

This method was implemented by Way (19); however, he found the system was unstable to limit cycle oscillations. This was a result of the fact that there is no restoring spring constant at zero applied torque. Method a, on the other hand, has finite stiffness in roll at zero angular error ($\theta = 0$)

since the AC field is fully energized at all times, not just when torque is being called for by the control system.

This system was tested by converting the roll drive circuit of Way (19) to one which produced the needed constant amplitude, single phase field which could be rotated through a 45 degree range by a compensated error signal. For this method a single phase, constant amplitude field B is applied transverse to the wind axis at a small angle δ to the plane of the model loop. The nominal angular position of the model is ϕ, as shown in Figure 14.

The angle δ is generated by the compensator and is represented by the compensated error signal. Referring to Figure 15,

$$\phi_1 = \delta + \phi, \quad |B| = b \tag{6}$$

which has components from the inner and outer saddle coils

$$B_i = \frac{b}{\sqrt{2}} (\cos \phi_1 + \sin \phi_1) \tag{7}$$

$$B_0 = \frac{b}{\sqrt{2}} (\sin \phi_1 - \cos \phi_1) \tag{8}$$

$$B_i = \frac{b}{\sqrt{2}} (\cos \delta \cos \phi - \sin \delta \sin \phi + \sin\delta \cos \phi + \cos\delta \sin\phi) \tag{9}$$

$$B_0 = \frac{b}{\sqrt{2}} (\sin \delta \cos \phi + \cos \delta \sin \phi - \cos \delta \cos \phi + \sin\delta \sin \phi) \tag{10}$$

For small angles $\delta << 1$ radian

$$B_i = \frac{b}{\sqrt{2}} (\alpha - \delta\beta) \tag{11}$$

$$B_0 = \frac{b}{\sqrt{2}} (\beta + \delta\alpha) \tag{12}$$

where

$$\alpha = \cos \phi + \sin \phi, \quad \beta = \sin \phi - \cos \phi \tag{13}$$

The torque on the loop can be estimated using Eq. (1) to be

$$\tau \propto |B|^2 \sin 2\delta \tag{14}$$

Normally $|B|^2 = b^2$ but since the $\delta \simeq \sin\delta$ approximation has been made, $|B|^2$ is given by

$$B^2 = B_i^2 + B_o^2 \tag{15}$$

$$= \frac{b^2}{2}(\alpha^2 + \delta^2\beta^2 - 2\alpha\delta\beta) + \frac{b^2}{2}(\beta^2 + \delta^2\alpha^2 + 2\alpha\delta\beta) \tag{16}$$

Therefore,

$$\tau \propto 2b^2(1 + \delta^2)\delta \tag{17}$$

and the stiffness with respect to δ is given by

$$\frac{\partial\tau}{\partial\delta} \propto 2b^2(1 + 3\delta^2) \tag{18}$$

Thus the stiffness at the set point is always non-zero and increases quadratically for $\delta \neq 0$. Furthermore, it is independent of ϕ.

$$\text{for } \delta << 1, \quad \frac{\partial\tau}{\partial\delta} \propto 2b^2 \tag{19}$$

If b is constant, the system behaves as a linear system for small perturbations and therefore cannot limit cycle. As the model moves to higher amplitudes. The experimentally observed limit cycle requires the existence of a product of a quadratic signal with the torque rate signal. The present model is too crude to show this phenomena.

A photograph of the model used for system development testing is shown in Figure 16. This is an ellipsoidal iron core with a copper loop attached to it so the loop axis can be inclined slightly to the ellipsoid axis. This method of construction was used successfully for an F-16 aircraft model with the loop forming the wing leading and trailing edges and the offset core located in the fuselage.

The circuit used to develop the modulation for the two roll power amplifiers is shown in Figure 17. Here the two position sensor outputs are available for selection depending on the model position. The selected position signal is compared to a reference and the error signal is fed out to the compensator circuit (not shown). The compensated error signal is then supplied in the appropriate sense to the x axes of the two multipliers used as modulators. The Y axes are supplied by a stable oscillator and a phase adjusting network used to compensate for the difference in phase lag between the two power circuits.

Compensator

Compensator circuits essentially similar to the other degrees of freedom were used with the addition of 400 Hz notch filters to remove pickup. The moment of inertia and torsional stiffness of the open loop system was determined by Ramohalli (21). He found that for this model (Figure 16) the moment of inertia $J = 3.1 \times 10^{-5} kg\,m^2$. With the maximum current of 18 amperes $\tau = .00764$ N-m from the inner saddle coils alone. Since $T \alpha I^2$, linearizing about zero, we have $\partial T/\partial I = K_T I$. Hence, K_T is determined to be 0.00764/36 = 0.00042 N-m/amp. k,g and $1/\tau$ vary, depending on which coil system is being considered.

$$k_i = 4.07 \qquad k_o = 4.31$$

A control loop for one coil is shown in Figure 18 and the combined system for both coils is shown in Figure 19.

If a series compensator design is used, we have for the inner saddle (the outer saddle is similar except for a few parameters)

$$KG_cG_pH = \frac{K(s)(s + 140)}{s^2(s + 296.5)(s + 50)(s + 140)}$$

A root locus for this is shown in Figure 20 and the series compensator poles are listed below.

TABLE 2 Inner Coil Loop Parameters

K	k	Poles in minor loop configuration	Poles in series compensator configuration
$30^2(300)$	4.07	$-21.2 \pm 21.2j$	$-24 \quad \pm 21j$
$\frac{1}{2} \cdot 30^2(300)$	2.04	$-14.5 \pm 20.5j$	$-35.5, -12$
$2 \cdot (30^2)(300)$	8.14	$-26.5 \pm j20$	$-21 \quad \pm 37j$

Notice that in the minor loop feedback, Figure 19, the poles are not very sensitive to gain variations. However, we need rather large gains in the loops. In the series compensator we do not need the large gains, but for gain variations the poles are very sensitive and even go unstable. The minor loop has the advantage of being stable at all gains. It was the configuration that was successfully implemented.

System Operation

The error signal (after compensation) is fed directly to the summing point on the outer saddle channel. The error signal is also inverted and fed to the summing point on the inner saddle channel. The operating point (angle) is initially set using the position control pots P_2 and P_4, Figure 17.

The model position reference and response to various excitation phases is given below in Table 3. The position sensor outputs as a function of model angle are plotted in Figure 21. These are the x and y components of Figure 13 for zero pitch angle. Note that a different output and sign combination is needed for different zero position angles as indicated by the solid and dotted braces in Figure 21.

TABLE 3 Model Response to Different Roll Inputs

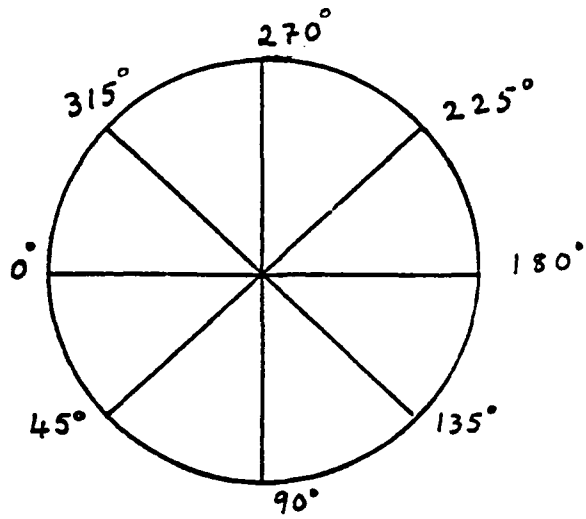

Model Position Reference

0° → Model loop horizontal above pivot in front and below pivot in rear.

Increasing angle → Rolling right wing up.

	Model	Angle
Inner saddle driven at 10V	135°	315°
Outer saddle driven at 10V	45°	225°
Inner + Outer in phase	0°	180°
Inner + Outer out of phase	0°	180°

The system was operated successfully with both the ellipsoidal model and the F-16 aircraft model. The range of roll angles was about 45 degrees for one setting of the control system as explained above. To extend this range, efforts were directed to implementation of digital control for the three angular degrees of freedom. This is discussed in the next chapter.

CHAPTER 5

INITIAL EXPERIMENTS WITH A MICROCOMPUTER AND THE MAGNETIC BALANCE

Initial experience operating the magnetic balance system with the analog roll control loop indicated that initial recommendations of Luh et al (14) and Way (19) that digital control for the system be implemented were correct.

Plans were then made to utilize an existing DEC 11-23 microcomputer with two additional Motorola 6800 microprocessors for data acquisition and digital control experiments. The work was planned in four steps:

1. Connect existing analog position and current outputs and position set inputs to the MINC 11-23 to provide digital data readout and position control on the analog system.

2. Check out system operation and verify choice of components while taking data.

3. Design microprocessor architecture and software for control of roll, pitch, and yaw.

4. Install and test digital roll control.

Because step (1) required much more effort than anticipated, it was only possible to complete steps (1) and (2) of the work.

The planned system is shown in Figure 22. Here the MINC is used to provide long-term monitoring of model position and to quickly read current and position data and then transfer it to the disc. Data reduction was performed with the balance system off line. To alleviate the need for an extremely large fast microprocessor the separate dedicated MC 6800 units were selected with one for each degree of freedom. It later appeared that all four might not be required so only two were purchased. However, termination of the contract did not allow us to install and test them.

In step (1) the position and current outputs of the analog control system for the magnetic balance were connected with two 27-pair shielded cables to the Data-Translation A-D Boards at the MINC output. A block diagram for this system is shown in Figure 23. Here the computer receives inputs of model position from the electric position sensor and magnet current from the shunts in the coil circuits for lift, drag, slip, pitch and yaw. A series of experiments were then carried out measuring the pitch damping of the ogive cylinder model previously built for spinning and coning tests (16) using white noise excitation of the model in pitch (22). Also some measurements of the asymmetric side force on this model when held statically at angles of attack up to 30 degrees were made.

These results are of interest because they indicate the feasibility of measuring the dynamic derivatives without inducing large amplitude periodic model motions (which are difficult to induce with power limited equipment) using short streams of data and in a noisy environment.

In the case of the asymmetric side force at high angles of attack the same fast Fourier transform software was used to obtain the spectrum of the measured side force. It is hoped this data will shed some light on the nature of the flow causing this side force.

Pitch Damping Measurement Using Random Excitation

The procedure followed here was to adjust the model suspension to be very stiff in all degrees of freedom except pitch. The pitch position response to white noise excitation was then stored during a run and analyzed using the MINC. For this case all displacements except pitch are negligible and the equation of motion is approximated as:

$$J \frac{d^2\theta}{dt^2} + (D_M - M) \frac{d\theta}{dt} + (K_M - M_\theta)\theta = P(t)$$

where J = Moment of inertia about the center of rotation of the model

D_M = Damping due to the magnetic suspension feedback system

K_M = Stiffness due to the magnetic suspension feedback system

$P(t)$ = Pitch input driving function

and the aerodynamic forces have been approximated by $M_\theta \theta + M$. Note that for this pure pitching motion $\dot{\theta} \equiv \dot{\alpha}$ so the term $M\dot{\theta} = M_{\dot{\alpha}} x \dot{\alpha} + M_{\dot{\theta}} x \dot{\theta}$. Also, since q (nondimensional pitch rate) = $\ell_{ref} \dot{\theta}/2U_\infty$, $C_{M_q} xq = C_{M_{\dot{\theta}}} x\dot{\theta}$. Thus the term M is a combination of $\dot{\alpha}$ and $\dot{\theta}$ terms. Using LaPlace transform we can take advantage of the fact that the transform of $P(t)$, $P(\omega)$ = constant if $P(t)$ is white noise. In the experiment white noise was obtained from a generator connected to the control system. Hence, in the transform domain, $\theta(\omega)/\text{const} = 1/\left[J\omega^2 + (D_M - M)\omega + (K_M - M_\theta)\right]$. The bandwidth of the corresponding power spectrum $\Delta\omega = 2\omega_n \zeta$, where ω_n = the natural frequency, can be used to determine the aerodynamic damping in pitch.

$$\Delta\omega = \frac{(D_M - M)}{J}$$

With the wind off, $M = 0$ and we can measure D_M/J.

J, the moment of inertia, is easily measured either directly by torsional pendulum or by measuring the resonant frequency and torsional magnetic stiffness wind off.

Thus M can be determined by subtraction. (Note that M_θ; and hence C_M can be found in similar fashion from the natural frequency. However, sufficient data has not been obtained to determine the accuracy compared to the classical static approach.)

Then $C_{M_{\dot{\alpha}}} x\dot{\alpha} + C_{M_{\dot{\theta}}} x\dot{\theta} = \dfrac{M\dot{\theta}}{\frac{1}{2}\rho U_\infty^2 SD}$ or since $\dot{\alpha} = \dot{\theta}$

$$C_{M_{\dot{\alpha}}} + C_{M_{\dot{\theta}}} = \frac{M}{\frac{1}{2}\rho U_\infty^2 SD}$$

This method of determining pitch damping is not new; in fact, it is the basis of the free oscillation technique used for years in wind tunnels. What is new is that the combination of the magnetic suspension system with the minicomputer permits rapid acquisition of data with high resolution combined with very small random model motion.

It is also possible to exploit the capability of producing a wide variety of model motions. For example, by applying the above technique in lift and side slip, C_{L_α}, $C_{L_{\dot{\alpha}}}$ and C_{Y_β} and $C_{Y_{\dot{\beta}}}$ can be determined. This can of course be done about zero degrees or about any desired angles of pitch or yaw.

Pitch Damping Data

The body tested was an ogive cylinder of 1 inch diameter and 5 inch length with a 1.506 caliber tangent ogive nose of 2.519 radius. This was the same body for which Magnus measurements were reported by Birtwell (9). FFT's of the wind off, wind on and digitally filtered wind on data are shown in Figures 24, 25 and 26. These were processed off line from data records containing 256 points of data recorded in one second. System response curves resulting from applying Ramohalli's data reduction approach (22) are shown in Figures 27 and 28. The resulting values for the damping coefficient ($C_{M_{\dot{\alpha}}} + C_{M_{\dot{\theta}}}$) are given in Table 4 as a function of wind speed for a white noise amplitude equivalent to 0.2 degrees pitch angle.

Data was taken on two model cores. One was a soft iron core and the other was a permanently magnetized samarium-cobalt core. This method was used to determine if the measured damping was being affected by hysteresis in the iron model. As can be seen from the data the model with the two cores gave results which were quite different. These results are shown in Figures 29-33 for the iron core and Figures 34-40 for the samarium-cobalt

permanently magnetized core. Figure 41 is a comparison cross plot of the 200 fps data versus angle of attack. These results differ so much that a shift in the control system induced magnetic damping from hour to hour is suspected. The most likely cause of this is inconsistent location of the analog system poles and zeros resulting from noisy connections or drifting components.

Because this method of determining dynamic stability derivatives depends on subtracting out the wind off response, any change in system performance function between wind off and wind on conditions is reflected directly as an error in the measurements. This initial experience indicates that the addition of a computer to the magnetic balance has greatly improved system versatility and data rate. The digital computer makes possible use of white noise excitation at small amplitudes for determining damping in pitch with much shorter run times than preceding methods. The technique should also be applicable for measurement of $C_{M_{\dot{\alpha}}}$ and $C_{L_{\dot{\alpha}}}$ from a pure plunging motion and $C_{N_{\dot{\beta}}}$ and $C_{Y_{\dot{\beta}}}$ from a slipping oscillation. Since the power demands are much lower than for forced oscillation testing, system operating range should be wider for this method of testing.

It has also demonstrated a need for greater stability of the analog control circuits before dynamic data accuracy can approach the level attained in static measurements. Digital control may be the best approach to improve stability. More effort is needed to develop this technique and also to apply the digital data system to determination of dynamic stability derivatives by direct instantaneous force measurement rather than by parameter identification methods.

While data was being taken at high angles of attack, some static measurements were made of the side force at 30 degrees angle of attack. These results are presented in Figure 42.

TABLE 4 Preliminary Pitch Damping Data for Ogive-Cylinder Model

Run	Angle of Attack α (degrees)	V ft/sec	$2\zeta\omega_n$	$C_{M_q} + C_{M_{\dot{\alpha}}}$ /deg
		Soft Iron Model		
Tare	2	0	66.5	----
1	2	50	71.4	-665
2	2	100	73.7	-489
3	2	200	69.5	-103
4	2	300	71.5	-113
Tare	4	0	70.9	----
1	4	50	65.6	+718
2	4	100	71.9	-67
3	4	200	86.6	-532
4	4	300	67.8	+71.6
Tare	8	0	80.0	----
1	8	50	77.1	+393
2	8	100	70.2	+666
3	8	200	64.9	+514
4	8	300	74.3	+131
Tare	16	0	73.6	----
1	16	50	66.2	+999
2	16	100	64.2	+637
3	16	200	68.1	+186
4	16	300	68.7	+111
Tare	32	0	73.4	----
1	32	50	83.2	-1300
2	32	100	79.7	-433
3	32	200	99.6	-893
		Samarium-Cobalt Model		
Tare	2	0	79.0	----
1	2	50	98.7	-2670
2	2	100	73.2	+392
3	2	200	66.3	+432
4	2	300	150	-1610
Tare	4	0	120	----
1	4	50	111	+1260
2	4	100	121	-54.4
3	4	200	119	+42.2
4	4	300	58.2	+1411

TABLE 4 (continued)

Run	Angle of Attack α degrees	V ft/sec	$2\zeta\omega_n$	$C_{M_q} + C_{M_{\dot{\alpha}}}$ /deg
Tare	8	0	105	----
1	8	50	95.4	+1360
2	8	100	93.0	+842
3	8	200	133	-936
4	8	300	98.9	+146
Tare	16	0	109	----
1	16	50	73.0	+4820
2	16	100	87.2	+1450
3	16	200	101	+250
4	16	300	104	+113
Tare	20	0	107	----
1	20	50	83.5	+3150
2	20	100	83.3	+1590
3	20	200	62.6	+1330
4	20	300	71.7	+793
Tare	24	0	77.4	----
1	24	50	109	-4280
2	24	100	76.3	+69.3
3	24	200	117	-1340
4	24	300	73.5	+87.9
Tare	28	0	84.3	----
1	28	50	95.4	-1500
2	28	100	71.9	+847
3	28	200	111	-913

Note: No transition devices were used on the model.

Chapter 6

Summary and Conclusions

During the research under this grant, study was directed toward the several areas of torque generation, position sensing, model construction and control system design. These efforts were then integrated to produce successful closed loop operation of the analogue roll control system. This experience indicated the desirability of microprocessor control for the angular degrees of freedom and work was started in this direction. It progressed through:

1. Connecting existing analog position and current outputs and position set inputs to the MINC 11-23 to provide digital data readout and position control on the analog system.
2. Checking out system operation and verifying choice of components while taking data on pitch damping.

This research indicated that:

1) The electro-magnetic position sensor (EPS) could be expanded to provide roll angle position information suitable for closed loop model control which was achieved.
2) The two phase AC method of torque production was capable of supporting an F-16 type model at aerodynamic loads consistent with the rest of the system. The available roll moment was limited by two factors a) high AC resistance in the saddle coils, b) limited roll power (2 kw/channel).
3) The EPS roll position output was a sufficiently complex function of model roll, pitch and yaw angles that microcomputer control is desirable for static tests and mandatory for dynamic tests.

4) The MINC 11-23 micro-computer used for pitch acquisition and model position set provided much better data resolution and about 10 times faster data rate than the analog system.

5) Additional work is needed to make control system stability and accuracy consistent with this new level of data resolution, particularly for dynamic tests such as pitch and yaw damping or measurement forces on a model undergoing complex motion such as spinning and coneing.

Recommendations

It is recommended that the original plan for implementing digital control in pitch, yaw, and roll be completed and additional computer facilities be added to permit the new range of dynamic testing to be explored.

The magnetic suspension and balance system provides the unique capability for sting-free testing of models undergoing complex motion. This appears to be the best method for measuring the results on flight vehicles of the complex aerodynamic phenomena associated with these motions. This capability should be exploited.

REFERENCES

1. Covert, E.E., M. Finston, M. Vlajinac and T. Stephens, "Magnetic Balance and Suspension Systems for Use with Wind Tunnels", Progress in Aerospace Science, 14, Pergamon Press, 1973, pp. 27-107.

2. Vlajinac, M. And E.E. Covert, "Sting-Free Measurements of Sphere Drag in Laminar Flow", Journal of Fluid Mechanics, 54, Part 3, Aug., 1972, pp. 385-392.

3. Judd, M.M., M. Vlajinac and E.E. Covert, " Sting-Free Drag Measurements on Ellipsoidal Cylinders at Transition Reynolds Numbers", Journal of Fluid Mechanics, 48, Part 2, July, 1971, pp. 353-364.

4. Vlajinac, M., T. Stephens, G. Gilliam and N. Pertsas, "Subsonic and Supersonic Static Aerodynamic Characteristics of a Family of Bulbous Base Cones Measured with a Magnetic Suspension and Balance System", NASA CR-1932, 1972.

5. McLaughlin, D.K., J.E. Carter, M. Finston and A.J. Forney, "Experimental Investigation of the Mean Flow of a Laminar Supersonic Cone Near Wake", AIAA Journal, 9, September, 1969, pp. 479-484.

6. Blankson, I.M. and M. Finston, "Measurements in the Laminar Near-Wake of Magnetically-Suspended Cones at M = 6.3", AIAA Journal, 13, No. 12, December, 1975, pp. 1562-1567.

7. Finn, D.M., C.W. Haldeman and E.E. Covert, "Wake Measurements behind a Magnetically-Suspended Spinning and Non-Spinning Ogive Cylinder at Angles of Attack", BRL CR 331, February, 1977.

8. Solomon, M., M. Finston and C.W. Haldeman, "Wake Studies Related to Reentrant Pyramids", MIT Aerophysics Lab. TR. 205, AFOSR-TR-79-0984, August, 1979.

9. Birtwell, E.P., J.B.Coffin, E.E.Covert and C.W.Haldeman, "Reverse Magnus Force on a Magnetically Suspended Ogive Cylinder at Subsonic Speeds," AIAA J 16, February, 1978, pp 111-116.

10. Bisplinghoff, R.L., J.B. Coffin and C.W. Haldeman, "Support Free Measurements of Aerodynamic Characteristics of a Spinning 2-1/8 inch Diameter Ring Airfoil using the Magnetic Balance", BRL CR 317, September, 1976.

11. Covert, E.E. and C.W. Haldeman, "Initial Wind Tunnel Tests of a Magnetically-Suspended Spinning and Coning Ogive Cylinder", MIT Aerophysics Lab. TR 201, DAAG29-75-C-0001, March, 1978.

12. Stephens, T., "Methods of Controlling the Roll Degree of Freedom in a Wind Tunnel Magnetic Balance. Part I: Production of Rolling Moments", U.S.A.F. ARL 65-242, MIT Aerophysics Lab TR 78, July, 1965.

REFERENCES (continued)

13. Stephens, T., "Design, Construction and Evaluation of a Magnetic Suspension and Balance System for Wind Tunnels", NASA CR-66903, MIT Aerophysics Lab TR 136, November, 1969.

14. Luh, P.B., E.E. Covert, H.P. Whitaker and C.W. Haldeman, "Application of Digital Control to a Magnetic Model Suspension and Balance Model", NASA CR-145316, January, 1978.

15. Haldeman, C.W., J.B. Coffin, E.P. Birtwell and M. Vlajinac, "Magnus Measurements with the Magnetic Balance System", BRL CR-153, MIT Aerophysics Lab TR 187, May, 1974.

16. Haldeman, C.W. and E.E. Covert, "New Techniques for Production of Combined Spinning and Coning Motion with Magnetically-Suspended Wind Tunnel Models", ICIASF Record, September, 1979.

17. Stratton, J.A., "Electromagnetic Field Theory", McGraw-Hill, 1941, p. 263.

18. Jahnke, E. and F. Emde, "Tables of Functions", Dover, 1945.

19. Way, Peter, A Roll Control System for a Magnetic Wind Tunnel Balance and Model Suspension System, S.M. Thesis, MIT, Department of Aeronautics and Astronautics, June, 1979.

20. Jung, W.G., "I.C. Op-Amp Cookbook", Howard W. Sams & Co., Inc., 1974.

21. Ramohalli, G., "Debugging the Roll Drive on the Magnetic Balance - a New Design for Better Performance", Interim memorandum AR 1043, February, 1981. (MIT Aerophysics Laboratory).

22. Ramohalli, G., "Stability Derivative Estimation using Digital Signal Processing Methods with the Magnetic Suspension Wind Tunnel", S.M. Thesis, Department of Aeronautics and Astronautics, MIT, May, 1981.

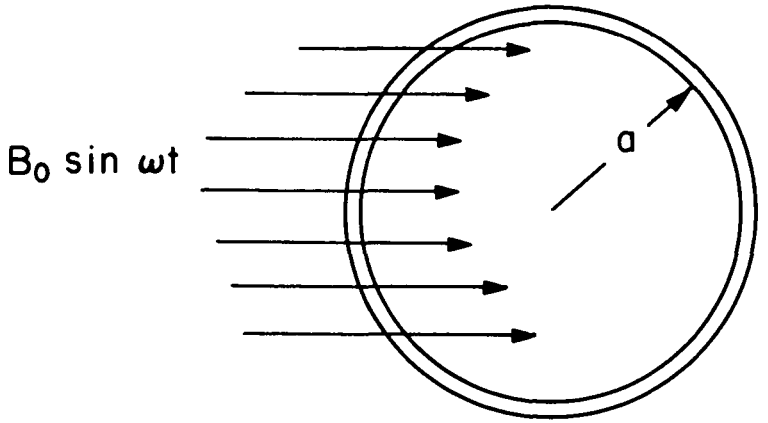

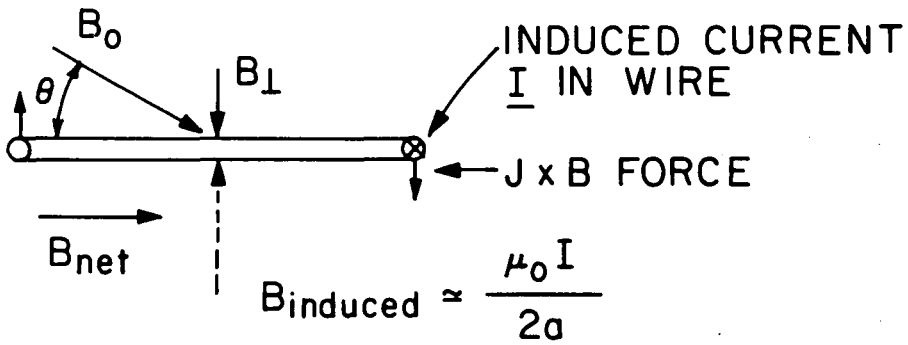

Figure 1 Circular Loop of Wire

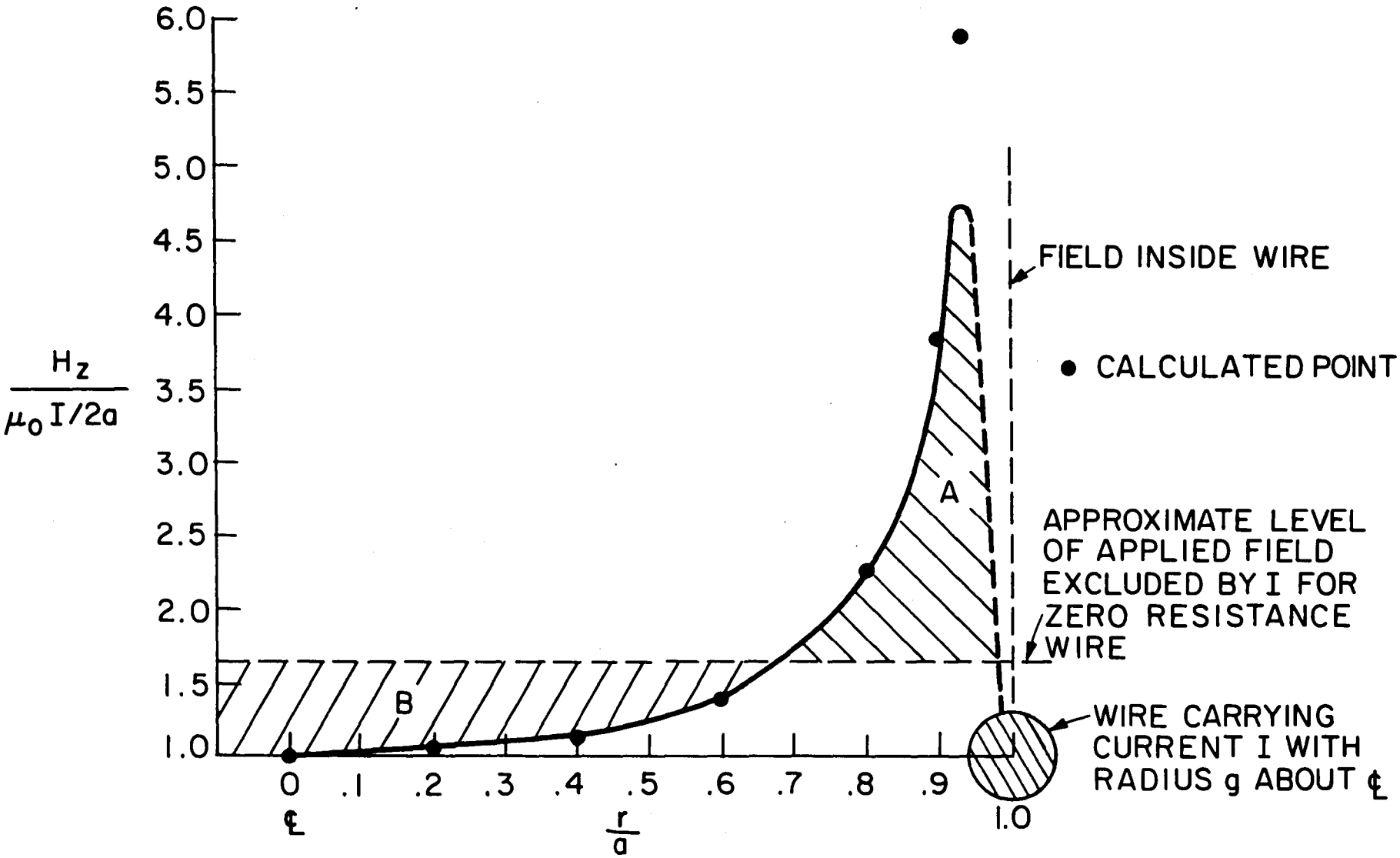

Figure 2 Field of a Circular Loop Current in the Plane of the Loop

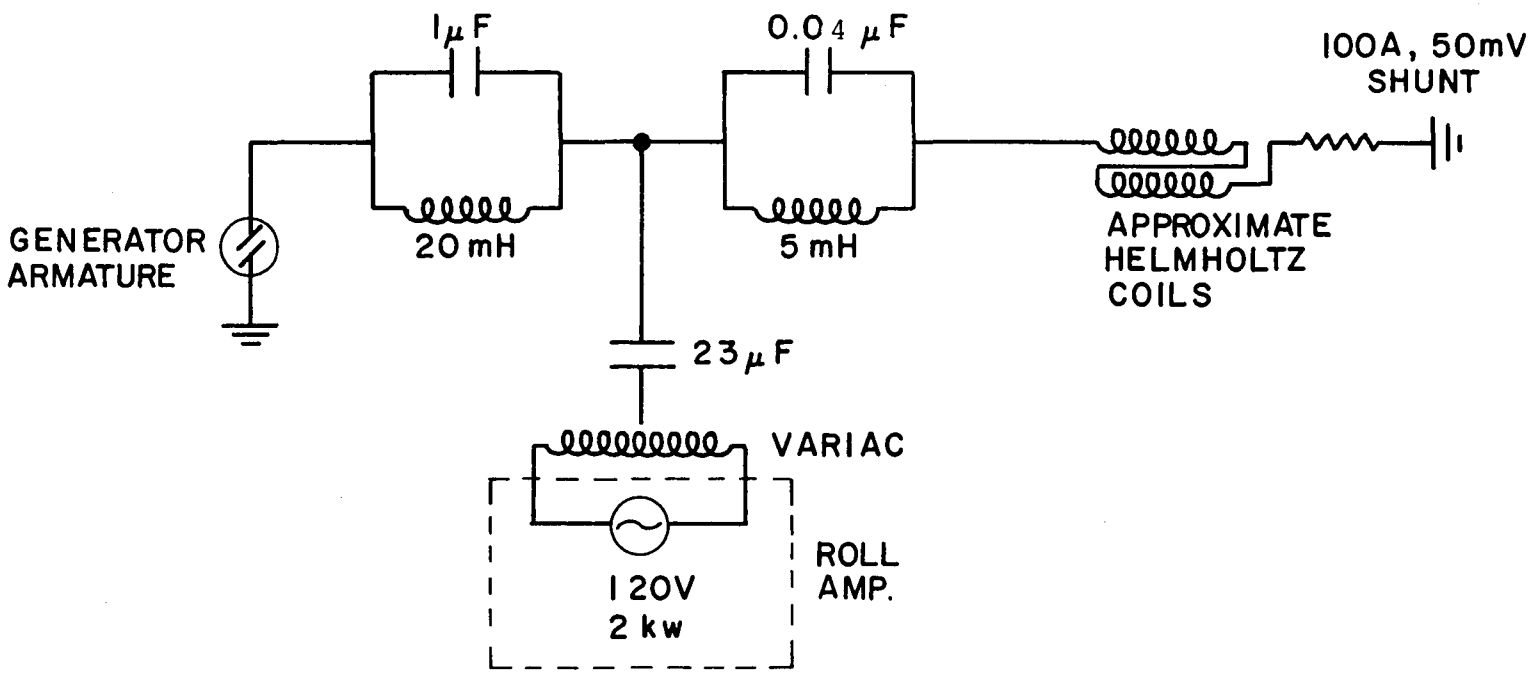

COIL CONSTANTS:

$R = 0.24\,\Omega$

$L = 8$ mH

$E = 360$ joules @ 300 A.

$B_y = 3.8\, I_y$

CIRCUIT CONSTANTS:

$L = 38$ mH

$R = 2.0\,\Omega$

$\frac{L}{R} = 0.019$ sec.

Figure 3 Inner Saddle Circuit

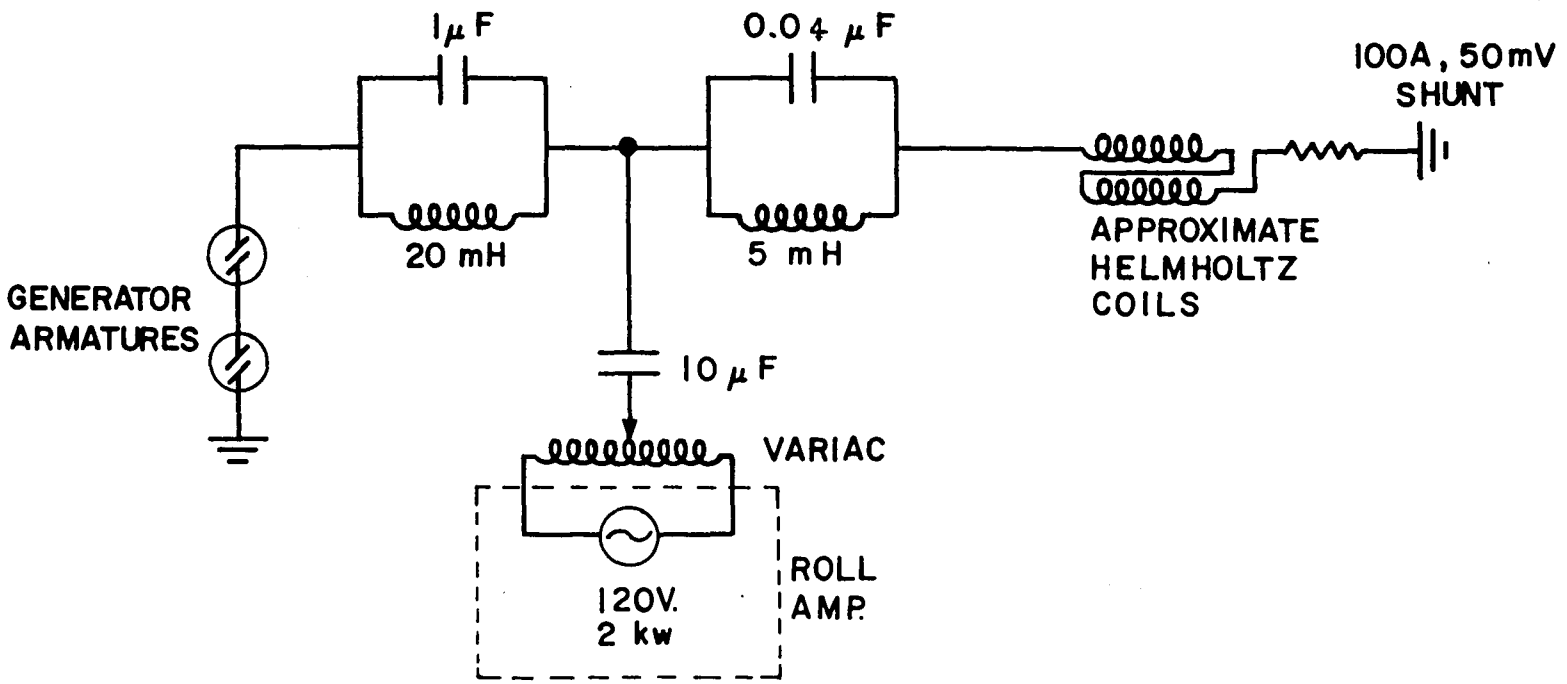

COIL CONSTANTS:

R = 0.44 Ω
L = 17 mH
N = 266 turns
E = 765 joules @ 300A.
$B_z = 3.5\ I_z$

CIRCUIT CONSTANTS:

L = 47 mH
R = 2.2 Ω
$\frac{L}{R}$ = 0.021 sec.

Figure 4 Outer Saddle Circuit

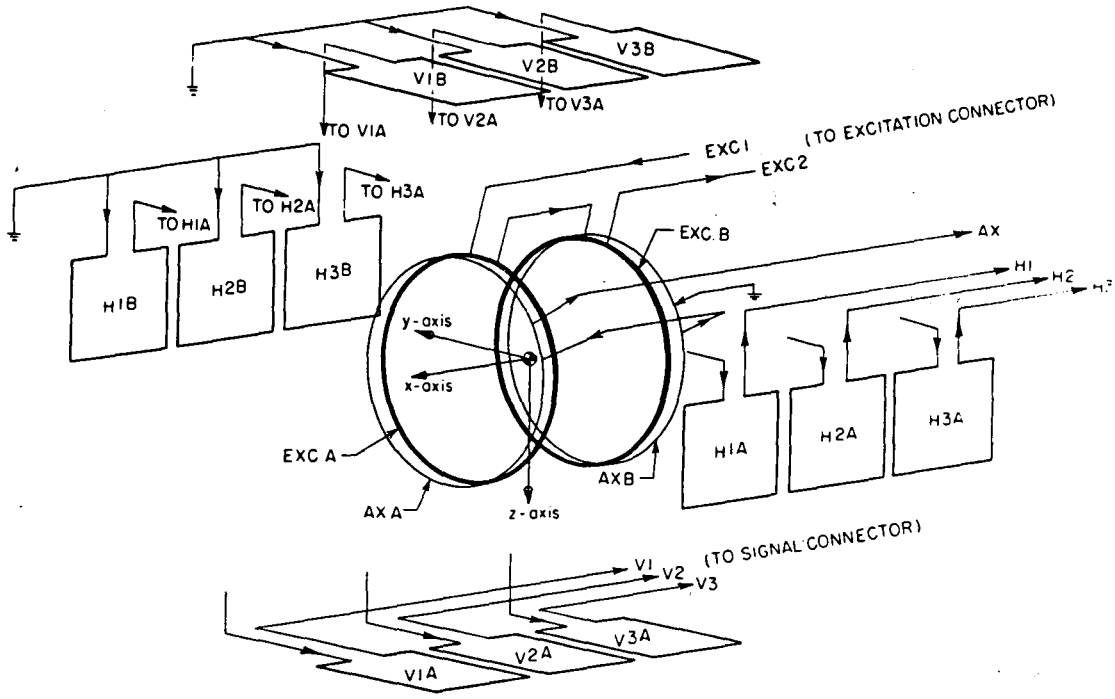

Figure 5 Pictorial of E.P.S. transducer coil windings

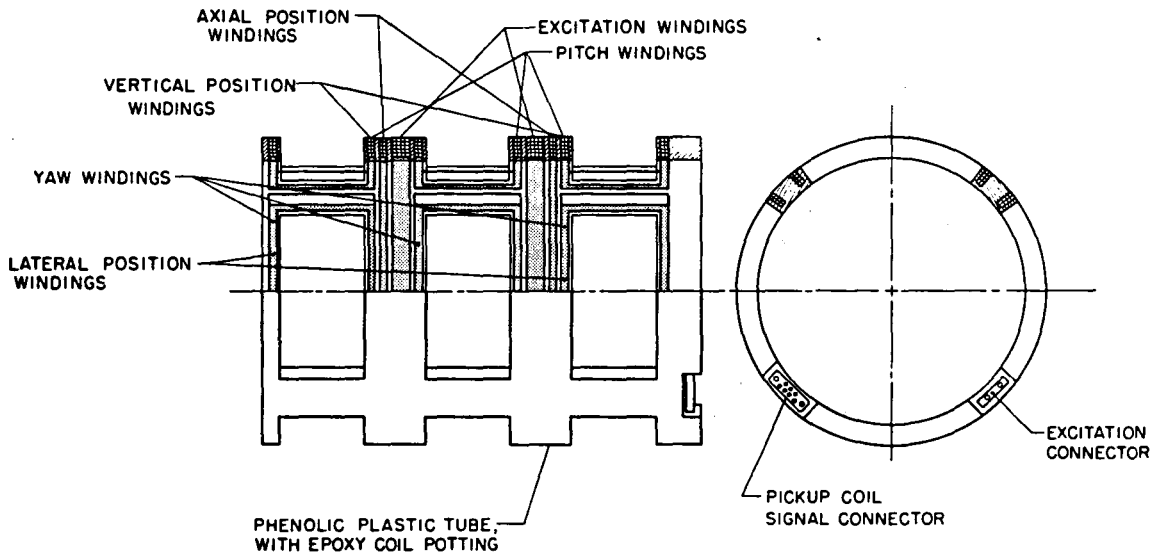

Figure 6 Sectional view of transducer coil

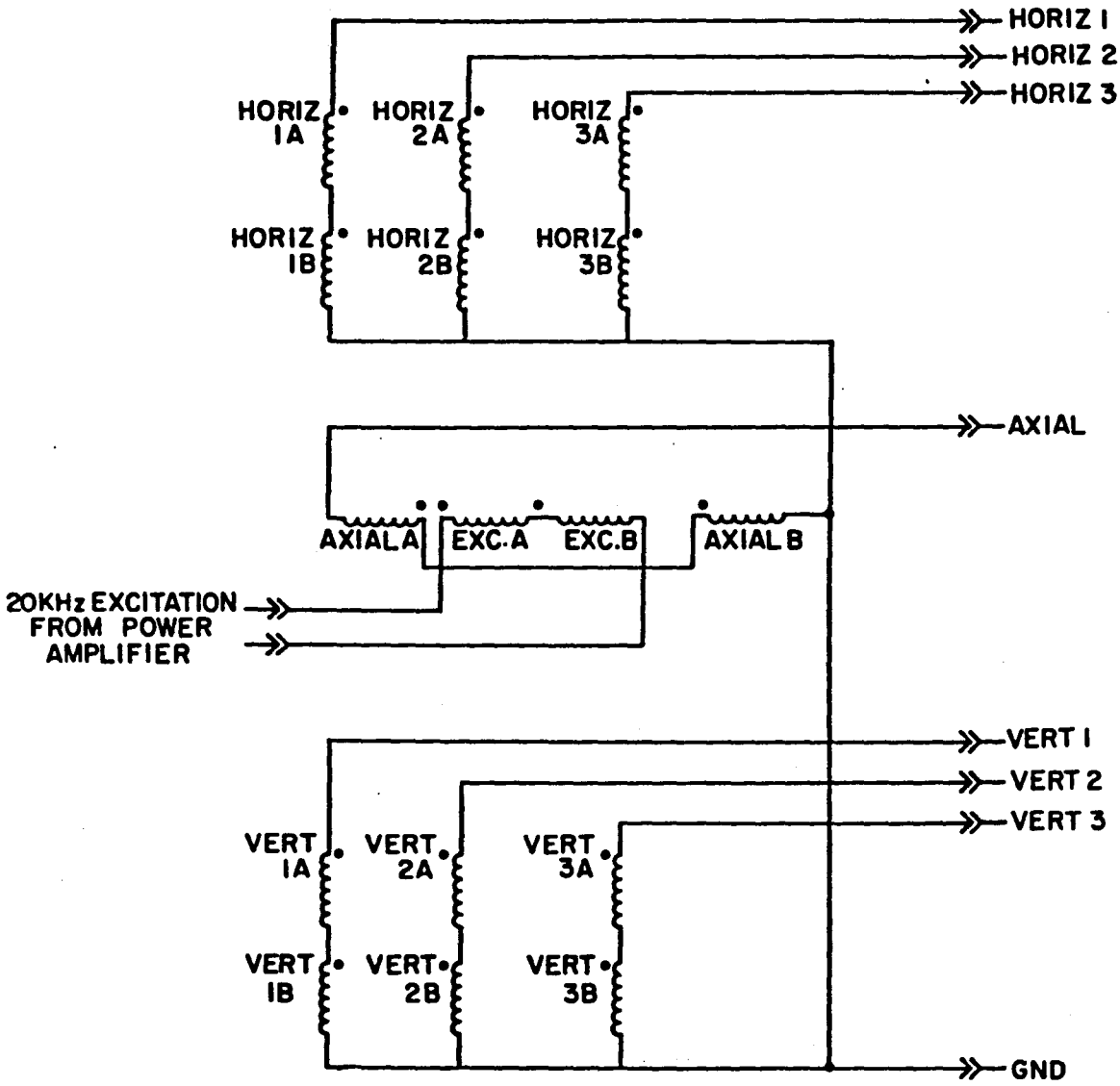

Figure 7 Schematic of E.P.S. transducer coils

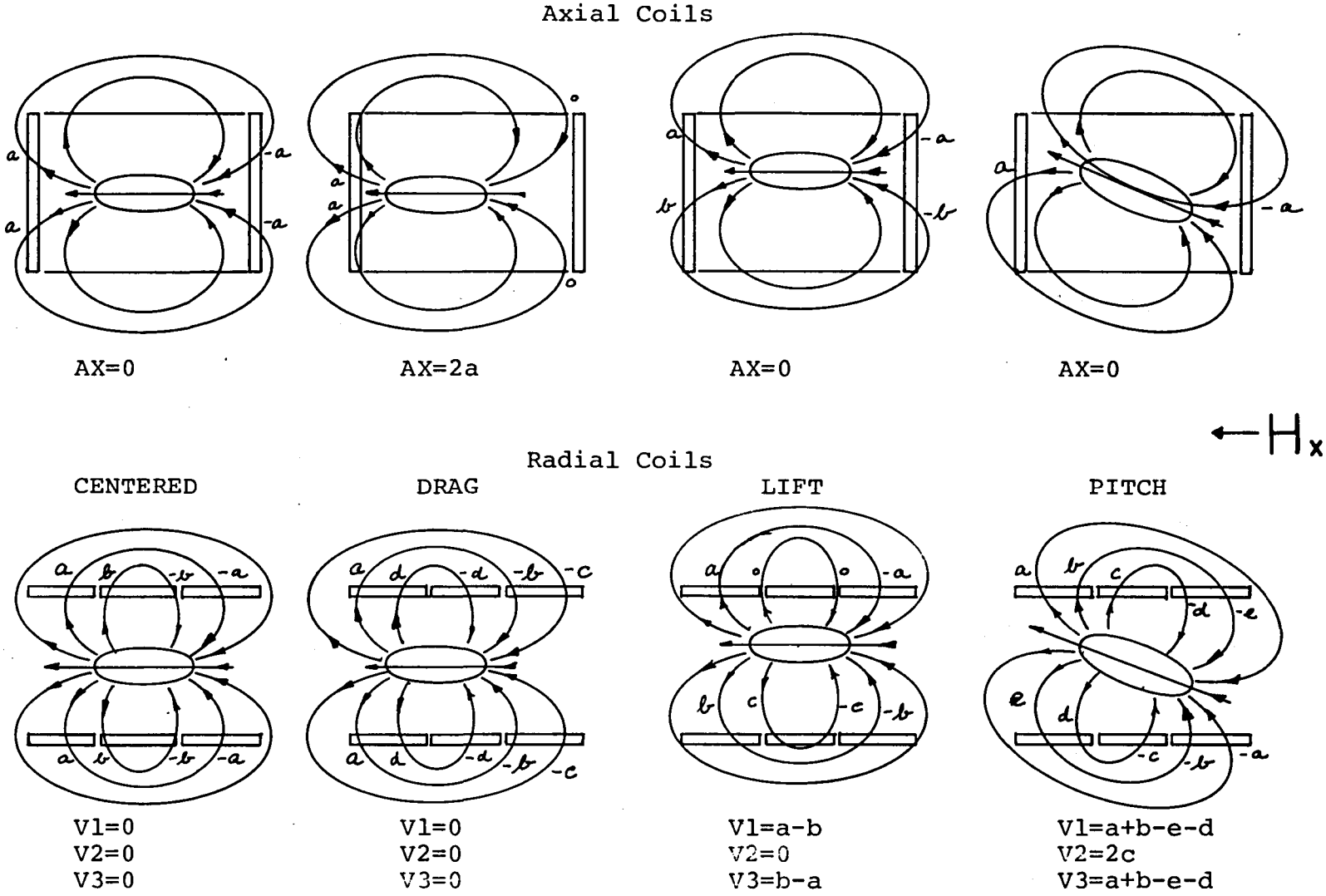

Figure 8 EPS signal contributions from single flux lines

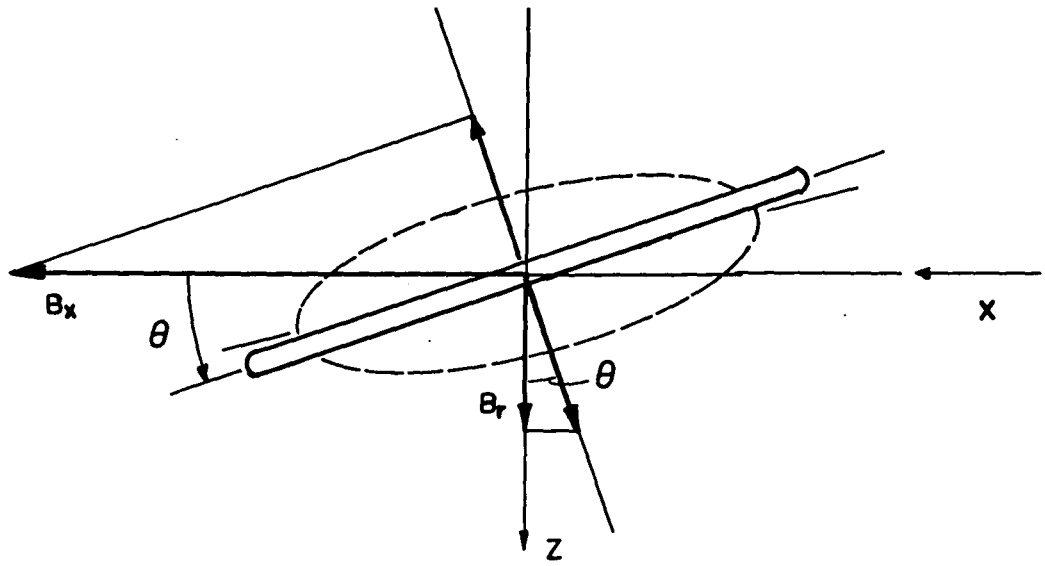

Figure 9 Radial Component of Field from a Conducting Loop in a Uniform Field

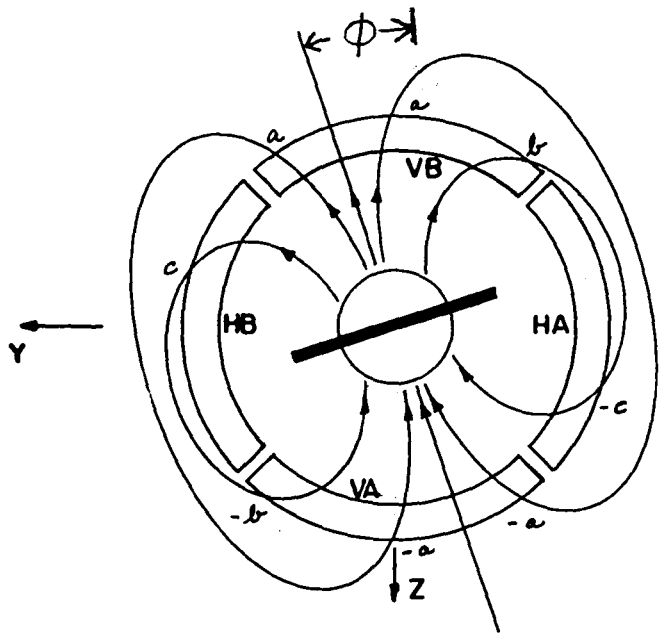

H=2c
V=4a+2b

Figure 10 Roll Signal Generation in the Pitch and Yaw EPS Coils

Figure 11 ROLL POSITION SENSOR BLOCK DIAGRAM
TWO REQUIRED

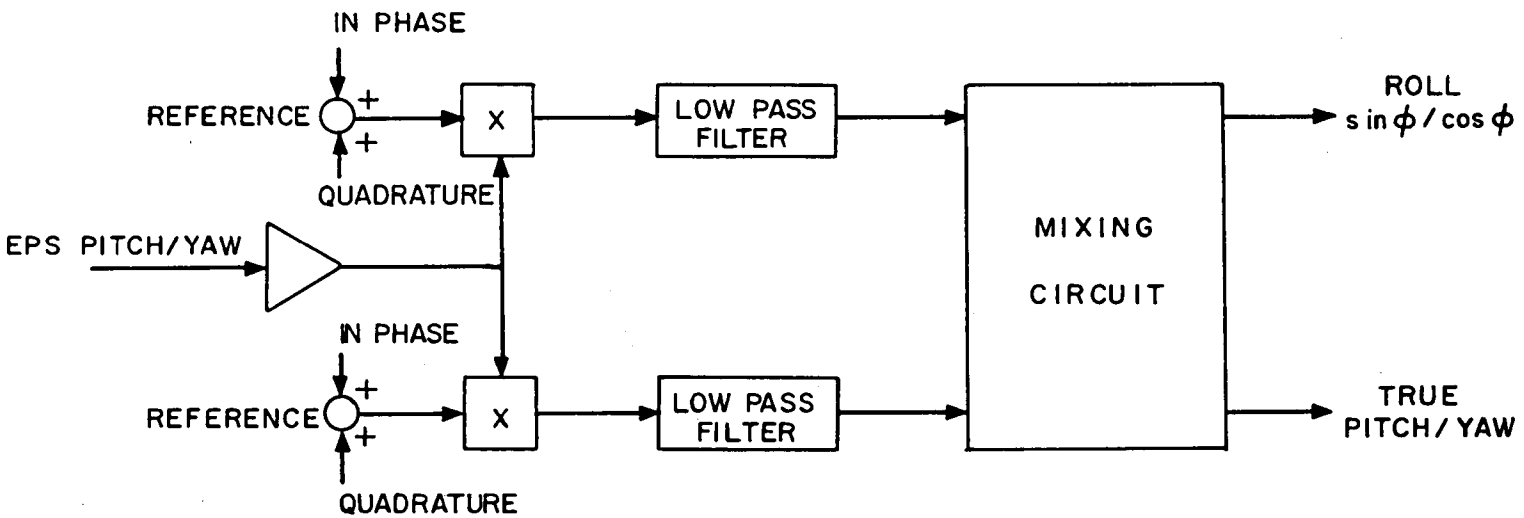

Figure 12 ROLL POSITION SENSOR CIRCUIT
(ONE OF TWO REQUIRED)

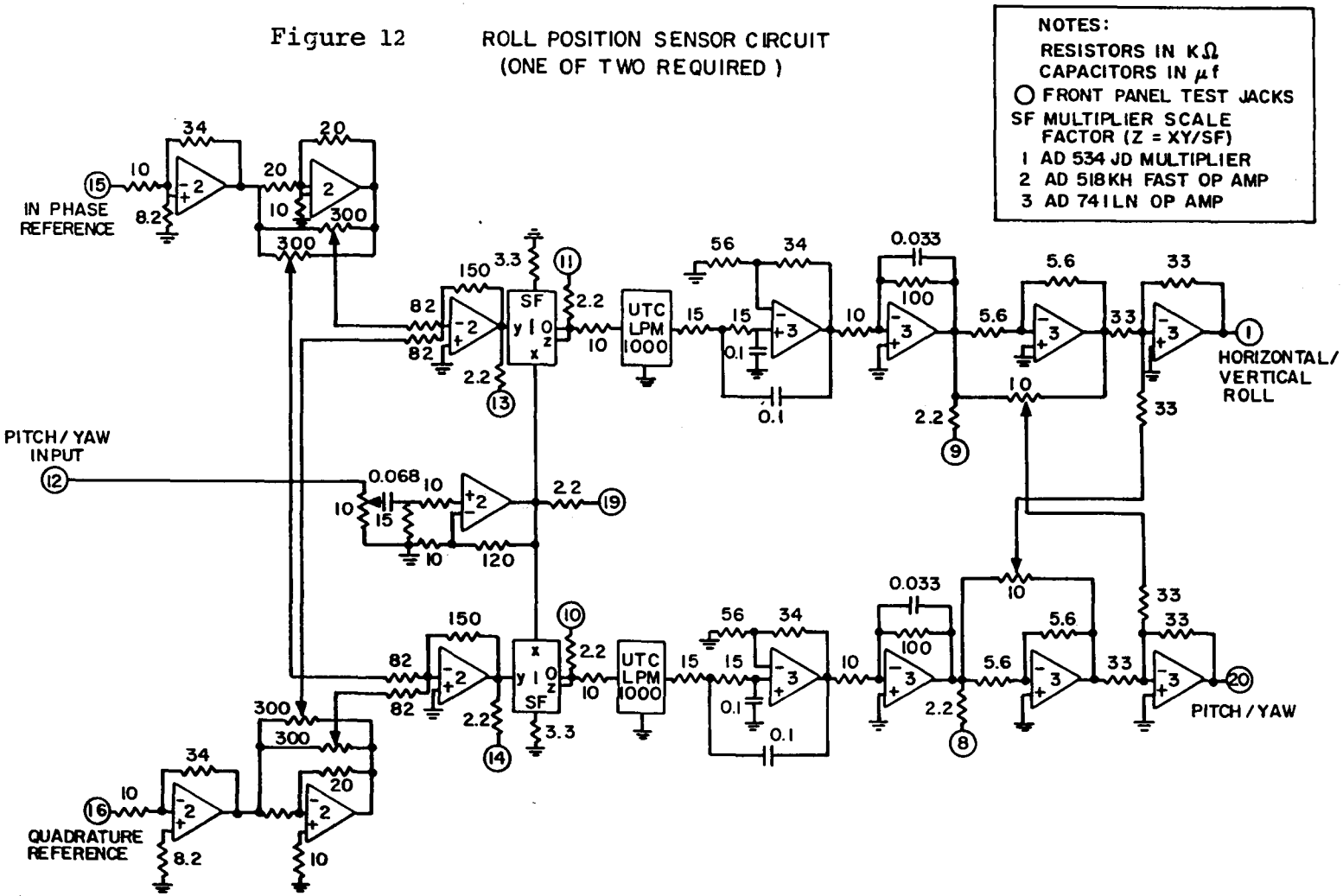

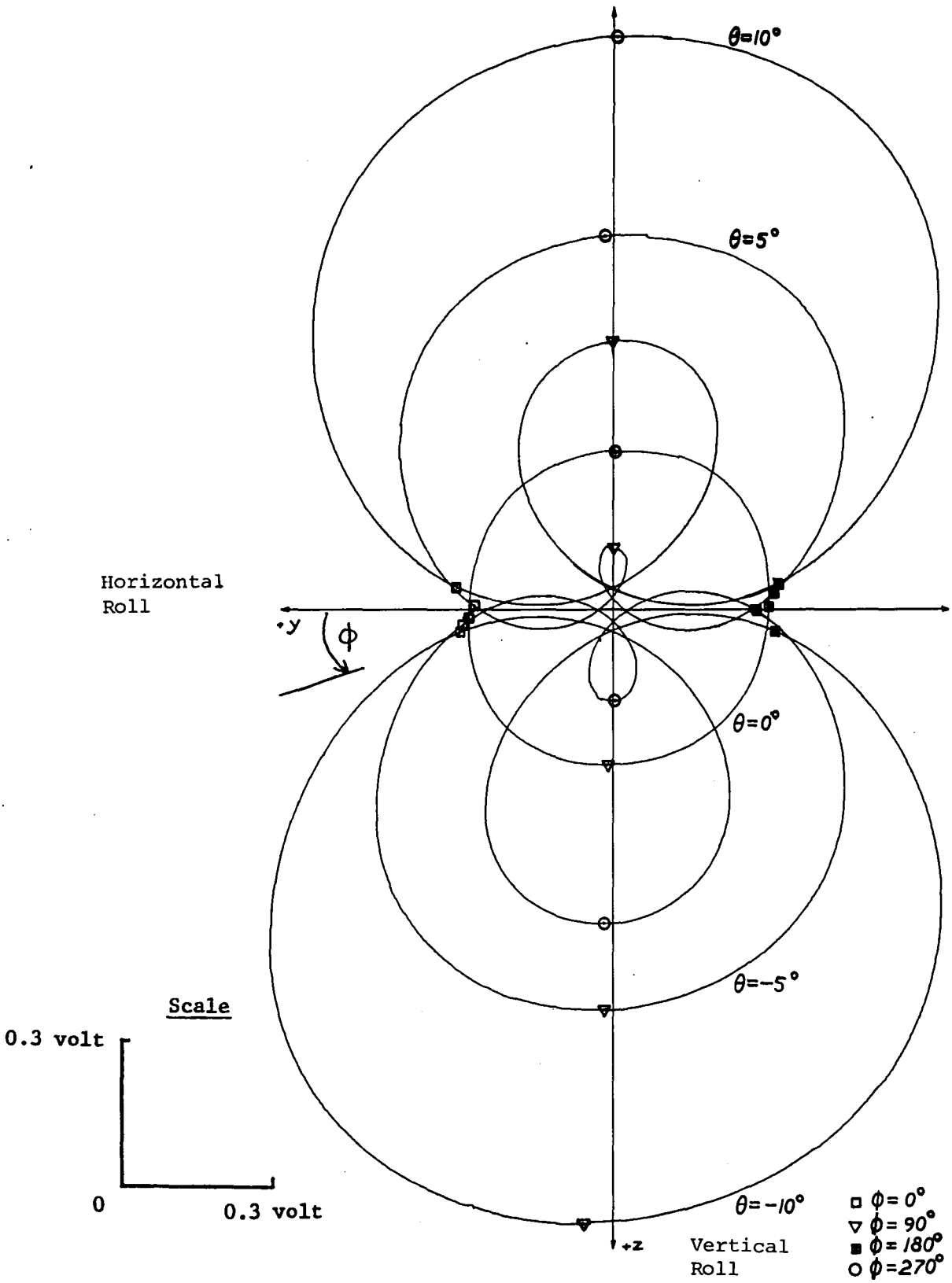

Figure 13 x-y Plotter Display of Roll Sensor Outputs as Model is Rolled at Various Pitch Angles

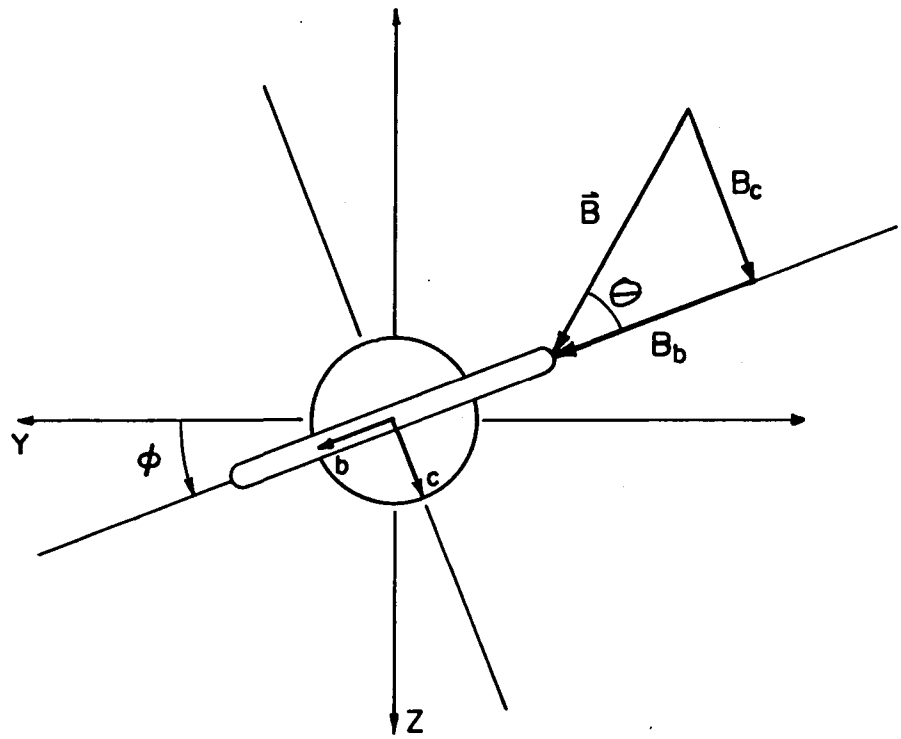

Figure 14 Transverse Field applied to a Model with a Roll Loop

FIGURE 15 RESOLUTION OF FIELD COMPONENTS

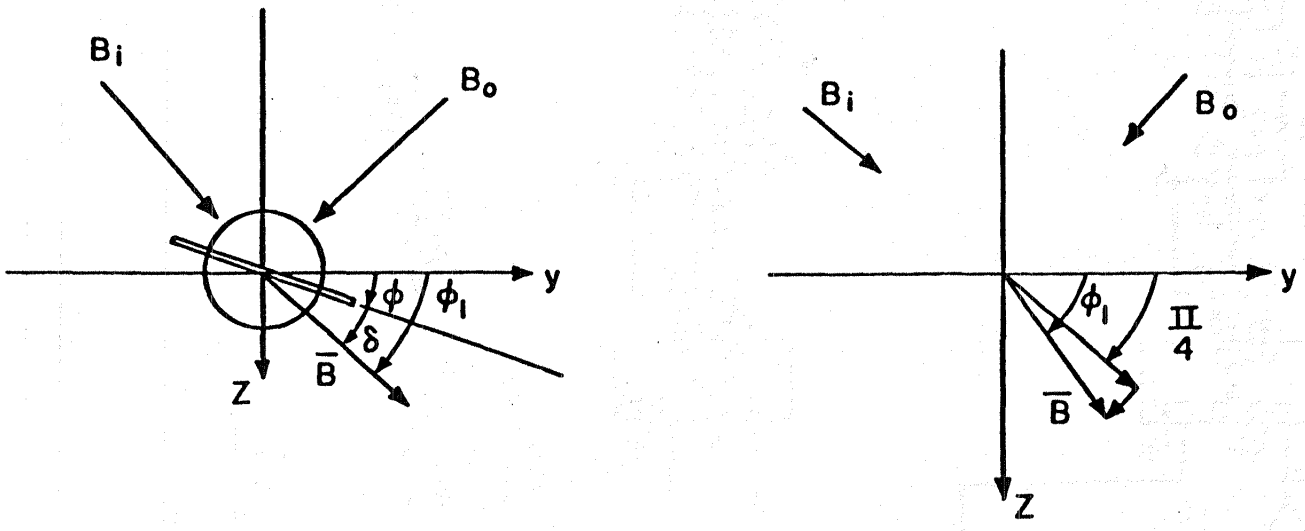

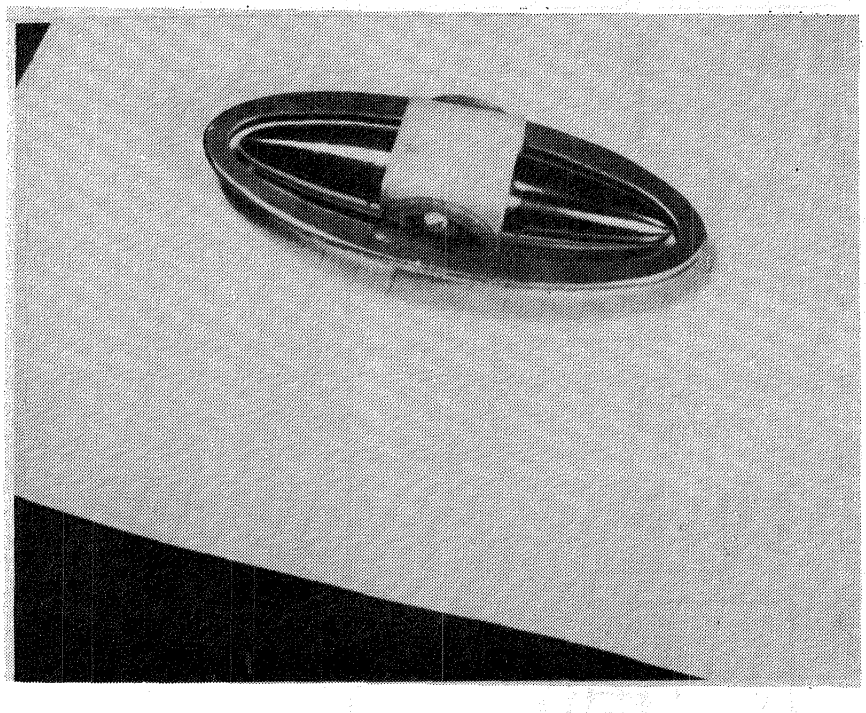

Figure 16 Ferromagnetic Model with adjustable Copper Roll Loop

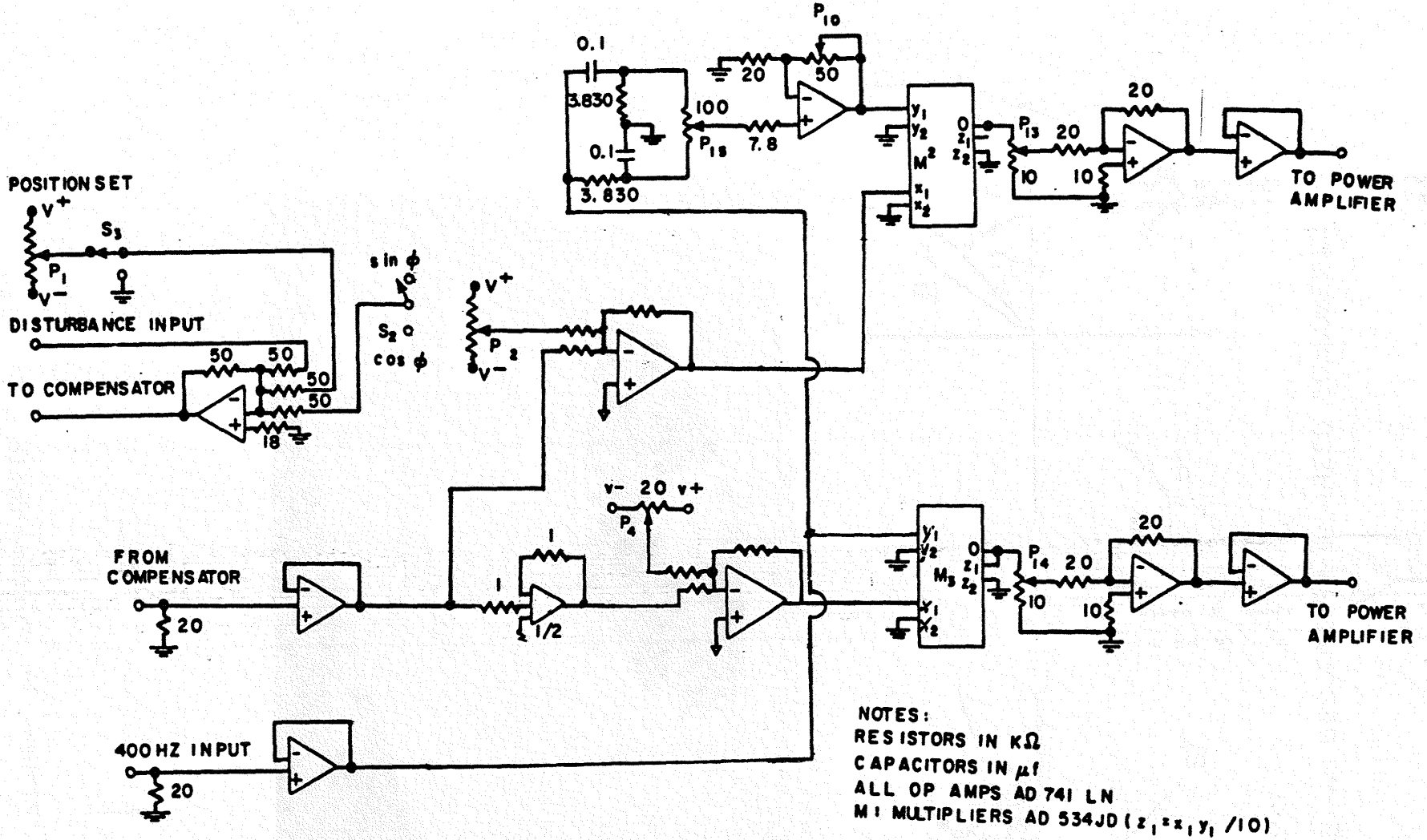

Figure 17 Simplified Roll Drive Circuit

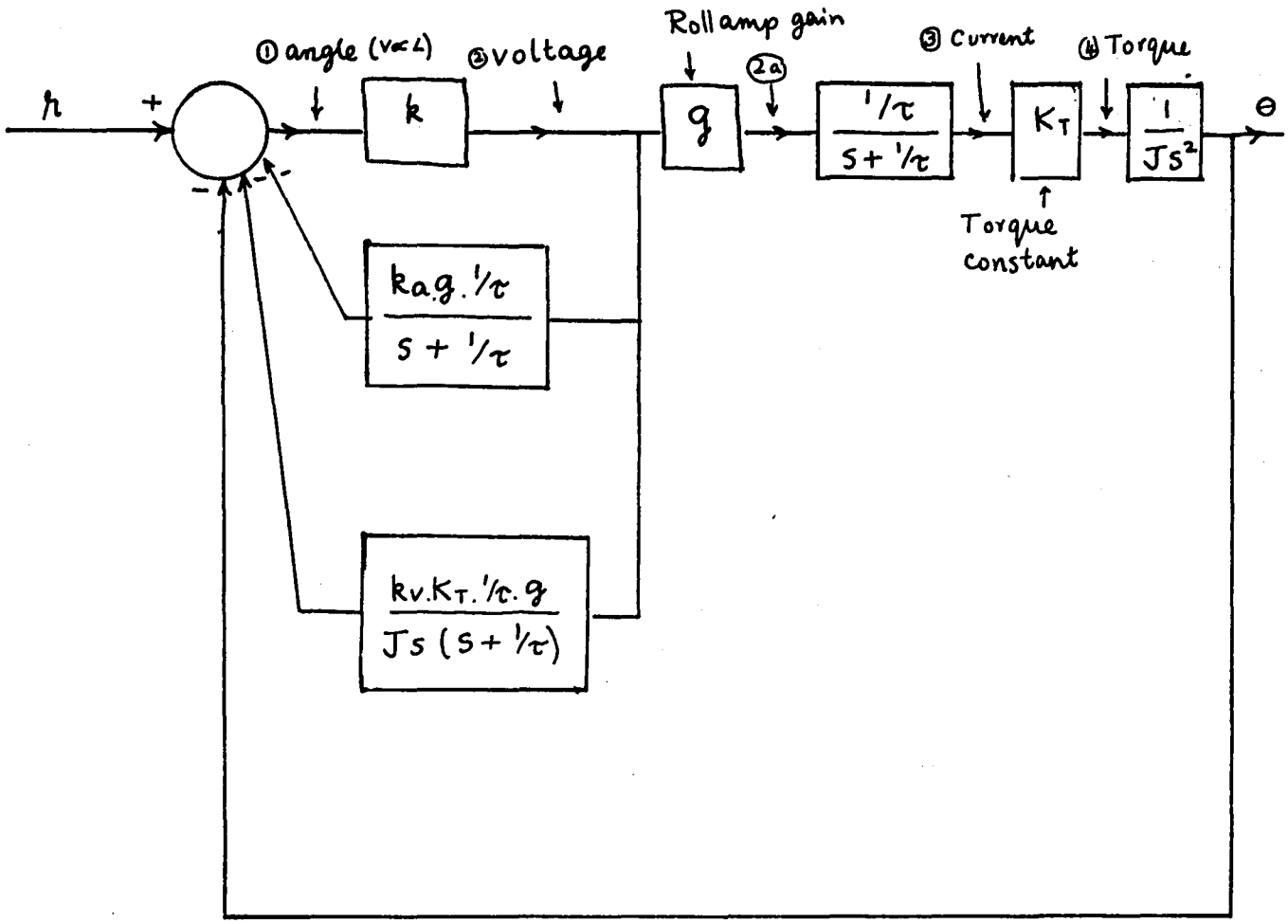

Figure 18 Block Diagram of Control Loop
(2 req'd; 1 per coil)

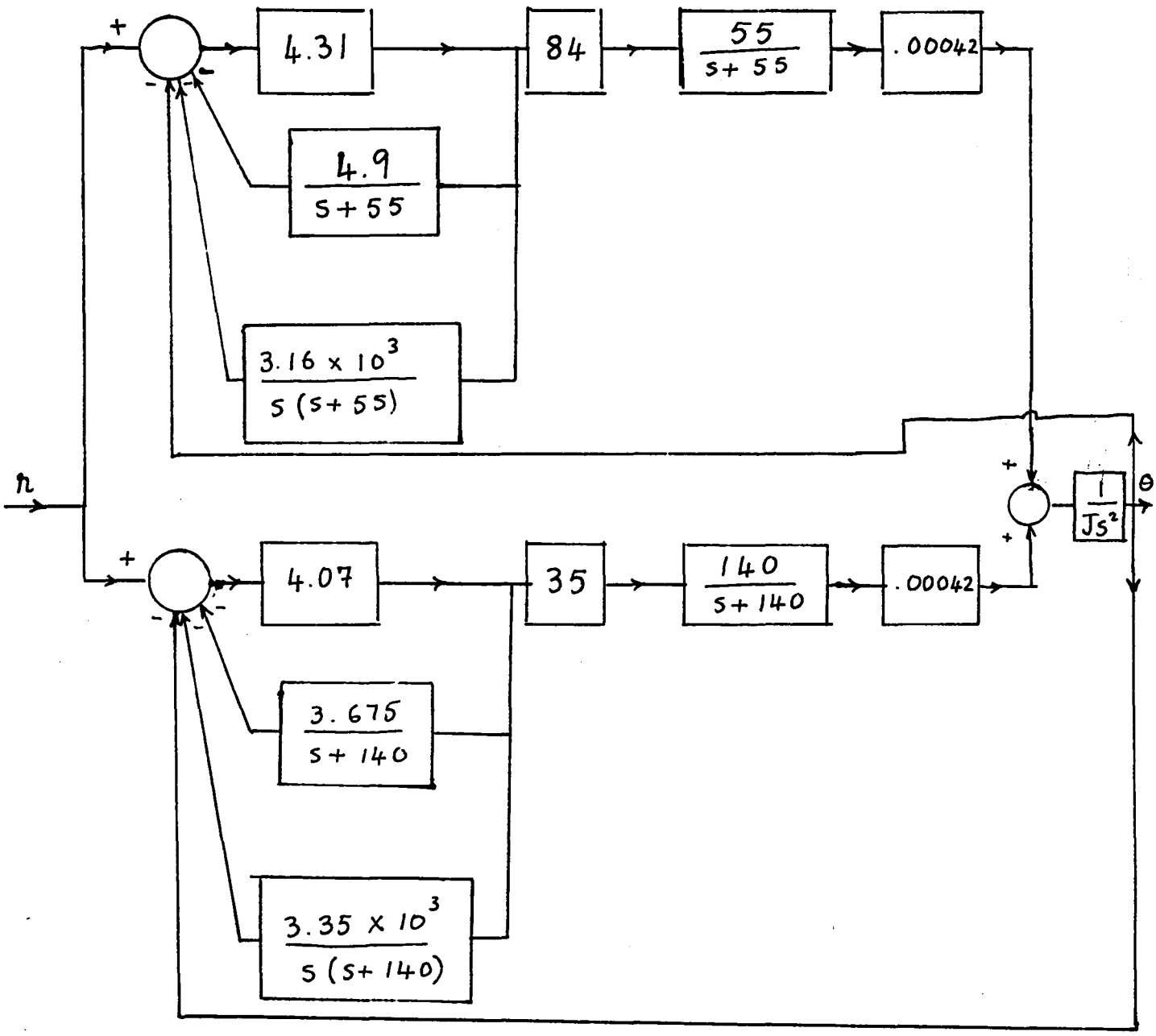

Figure 19 Control Loop for Both Coils with Proper Constants

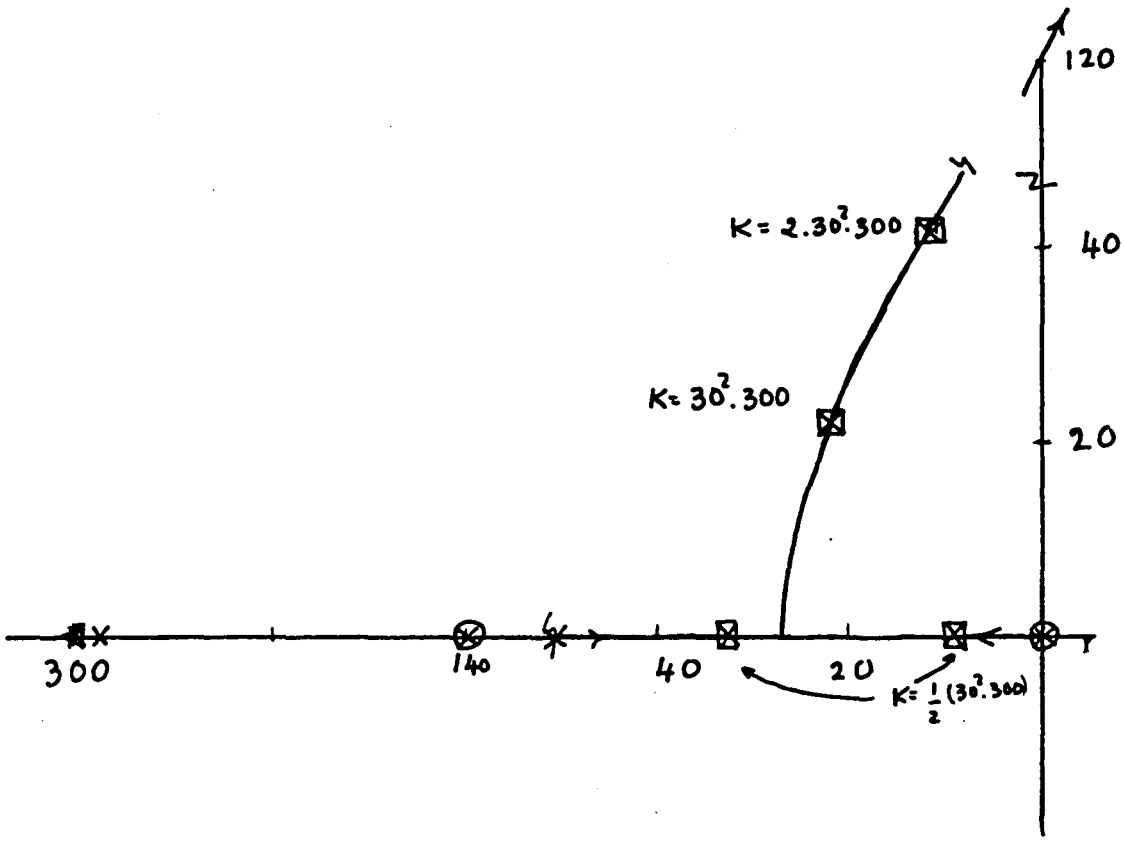

Figure 20 Roll Control Root Locus
Series Compensation

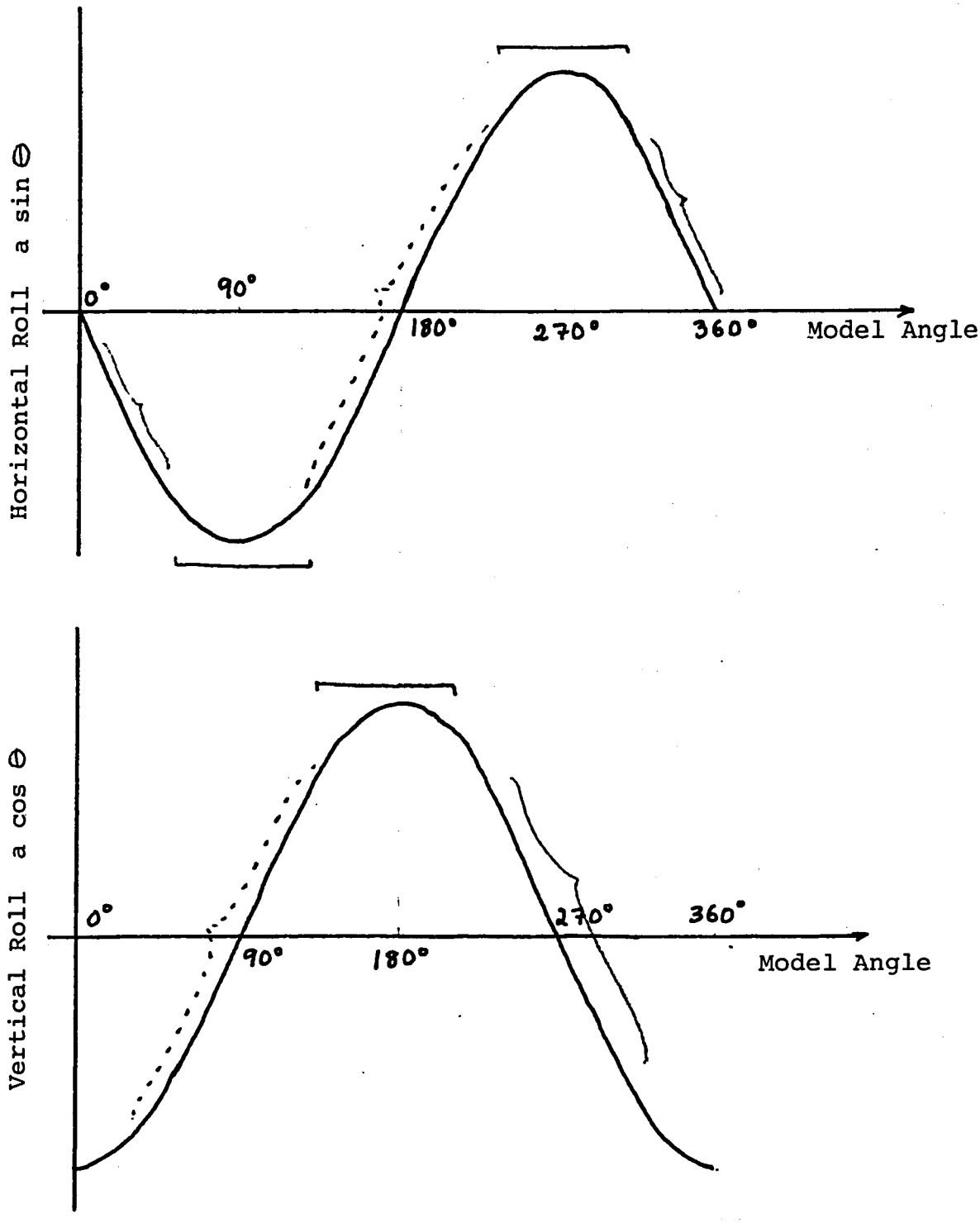

Figure 21 Roll Position Sensor Output Signals

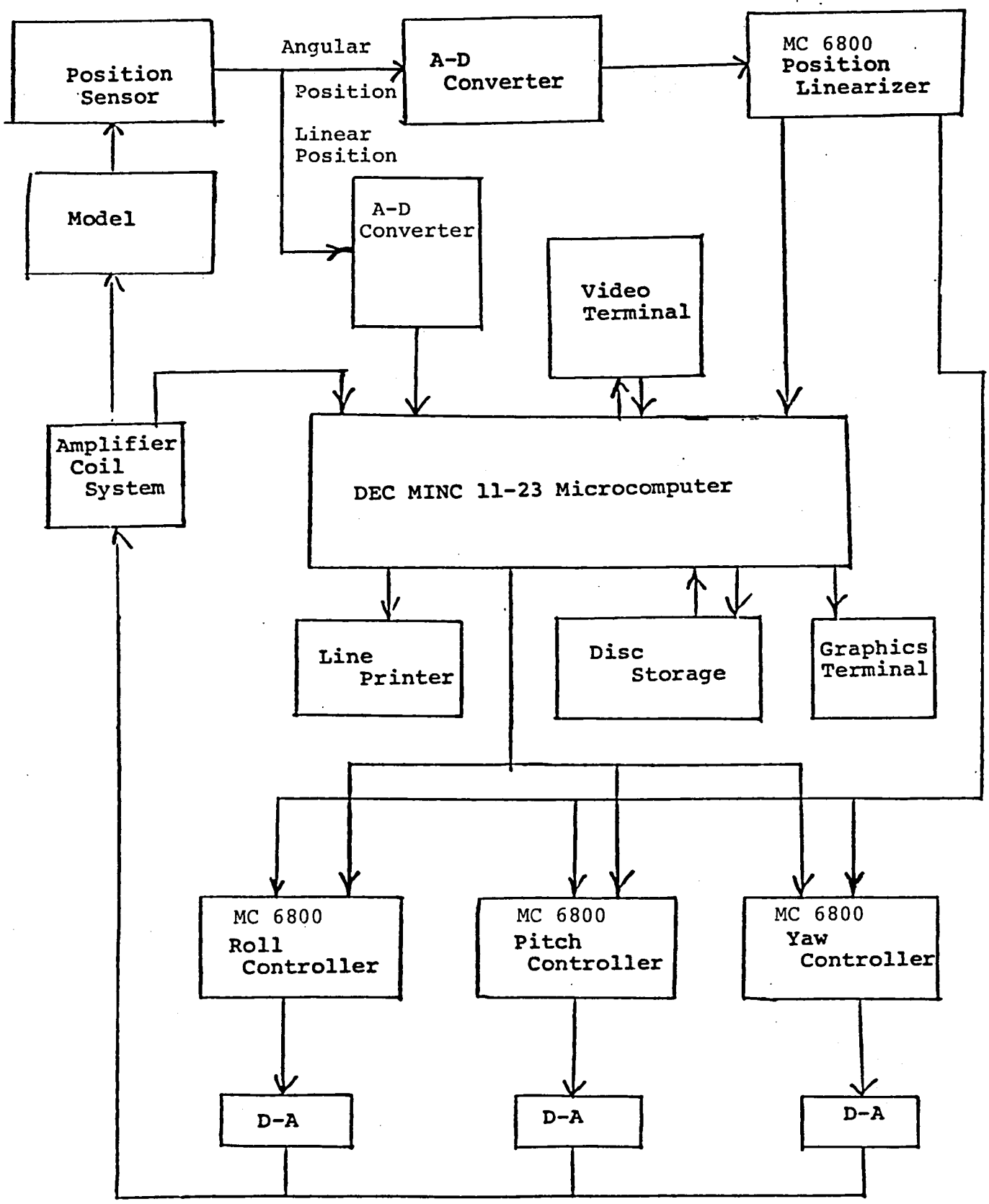

Figure 22 Block Diagram of Proposed Microprocessor Control System

Figure 23 Block Diagram of Computer-Magnetic Balance Combination

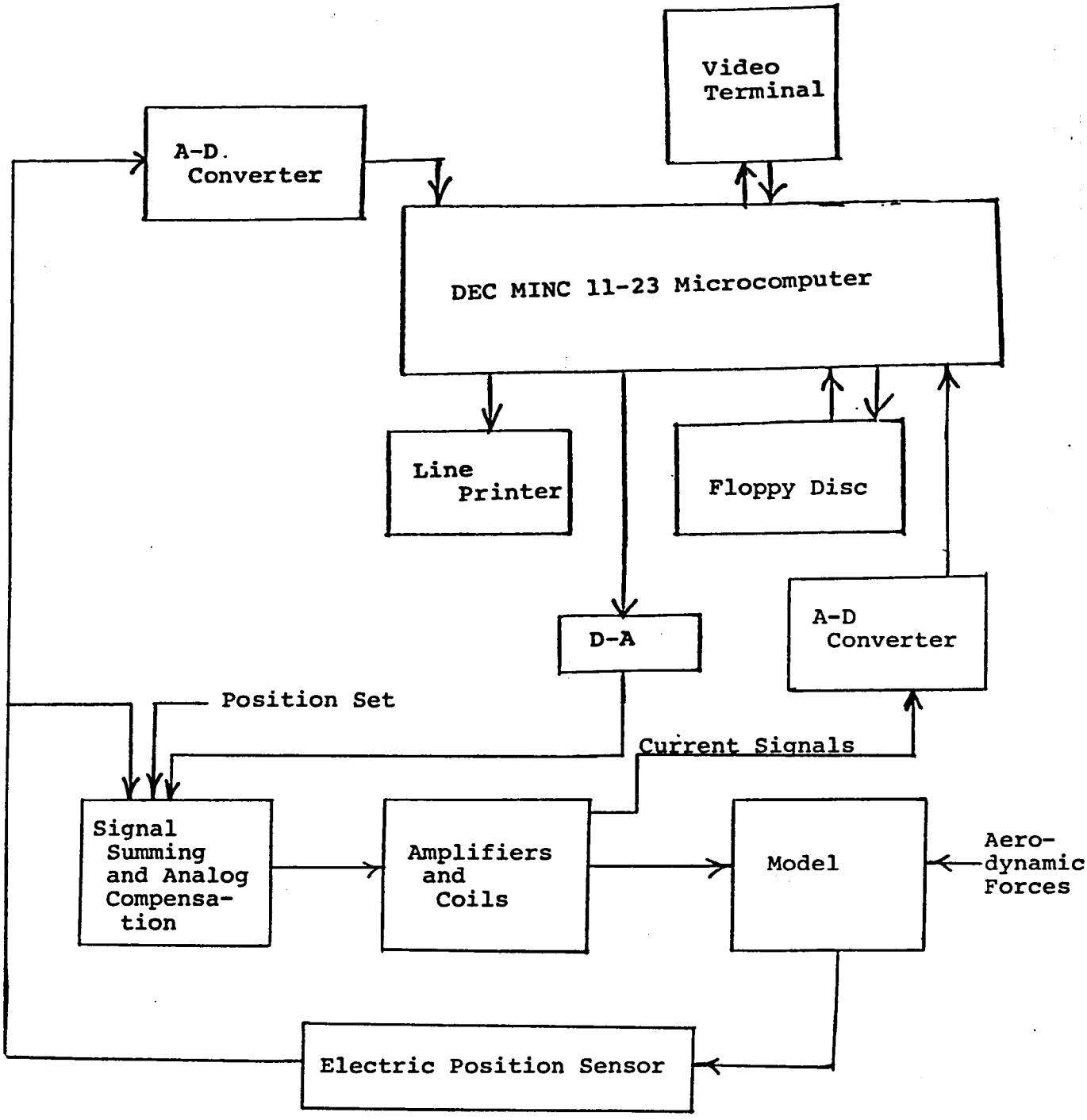

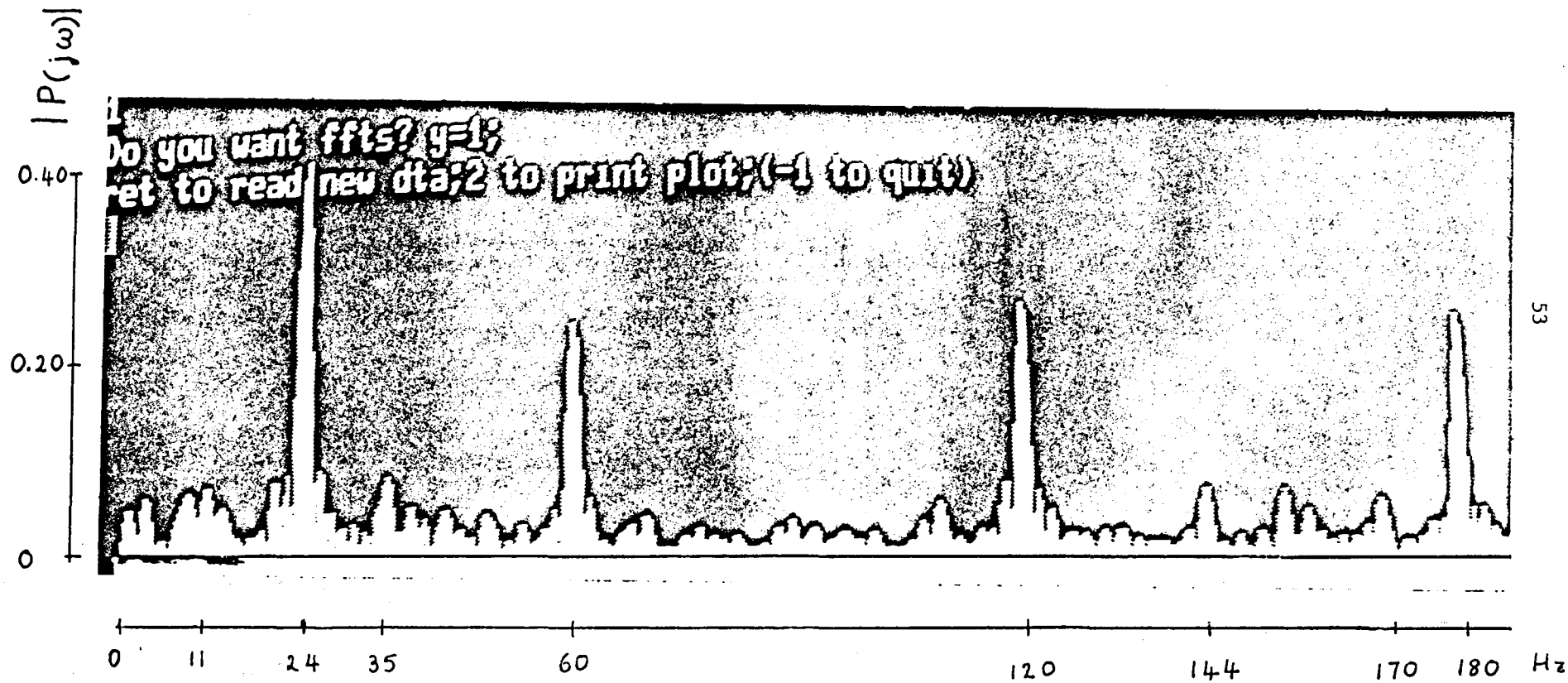

Figure 24 FFT of wind on noise off data.

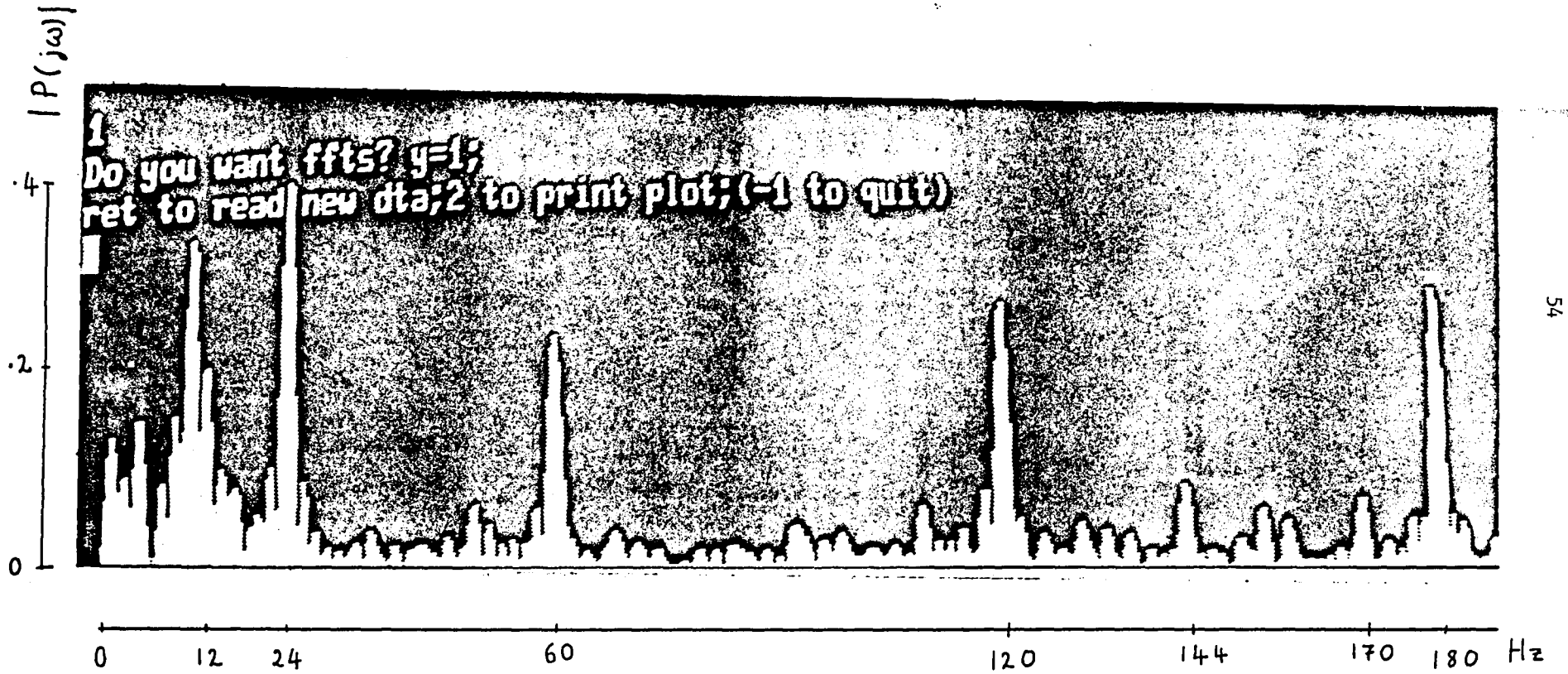

Figure 25 FFT of wind on noise on data.

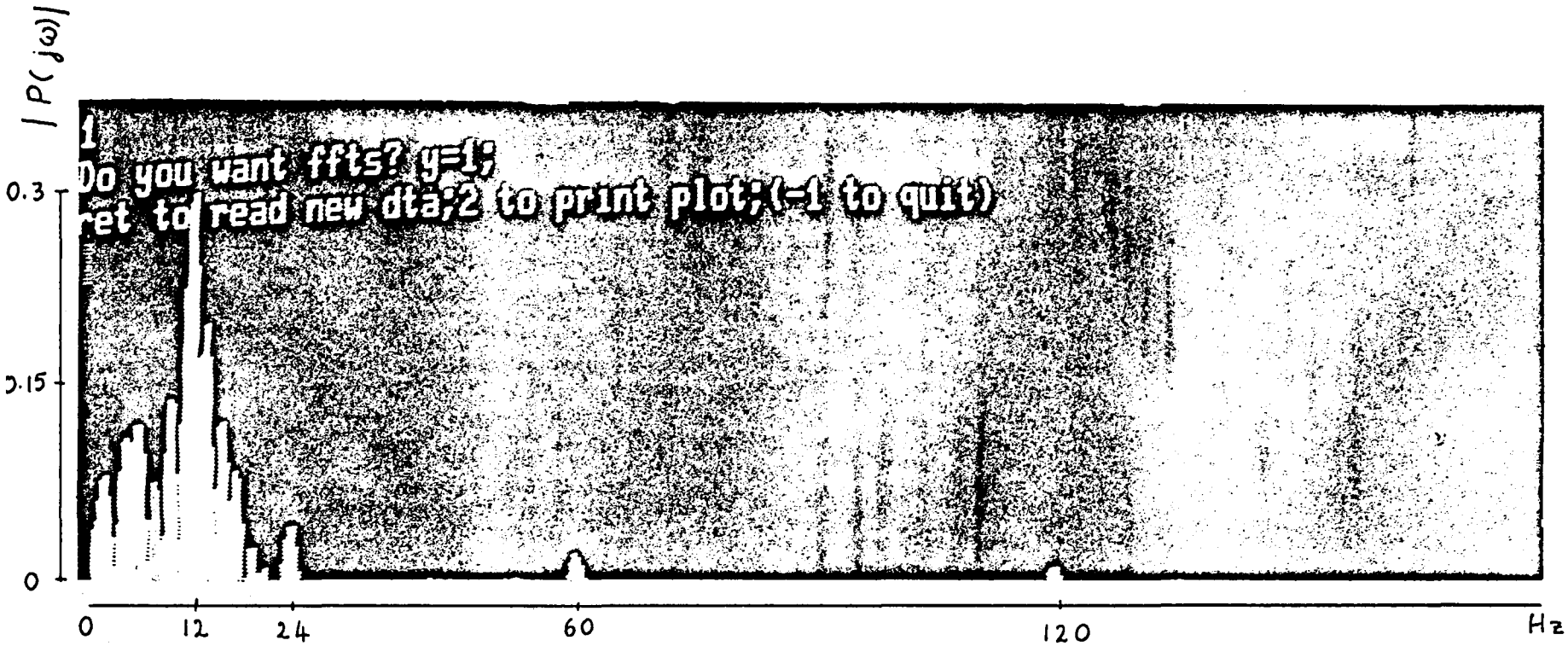

Figure 26 FFT of wind-on noise on data after filtering. The little peaks at 60 and 120 are due to the non-ideal nature of the filter.

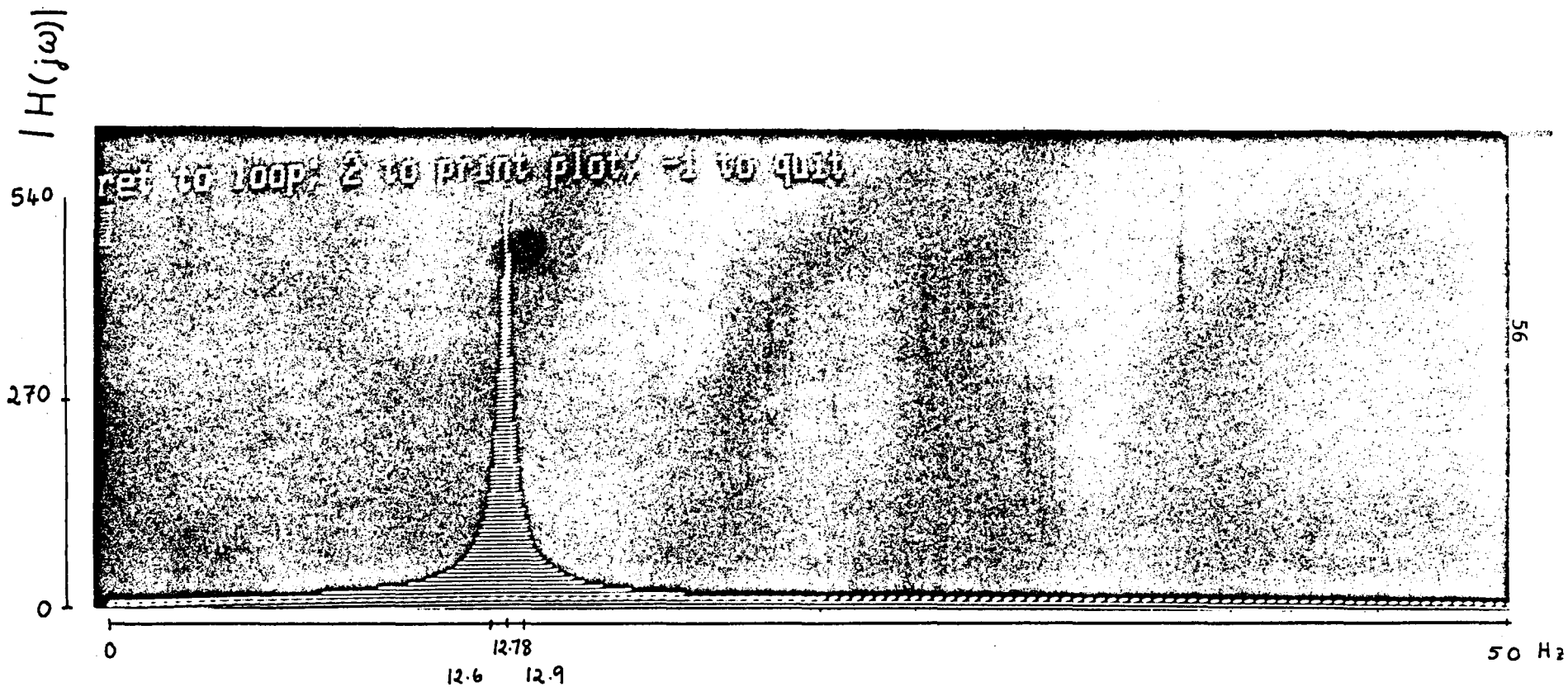

Figure 27 FFT of analytical model of the wind off data for 0.2°pitch noise.

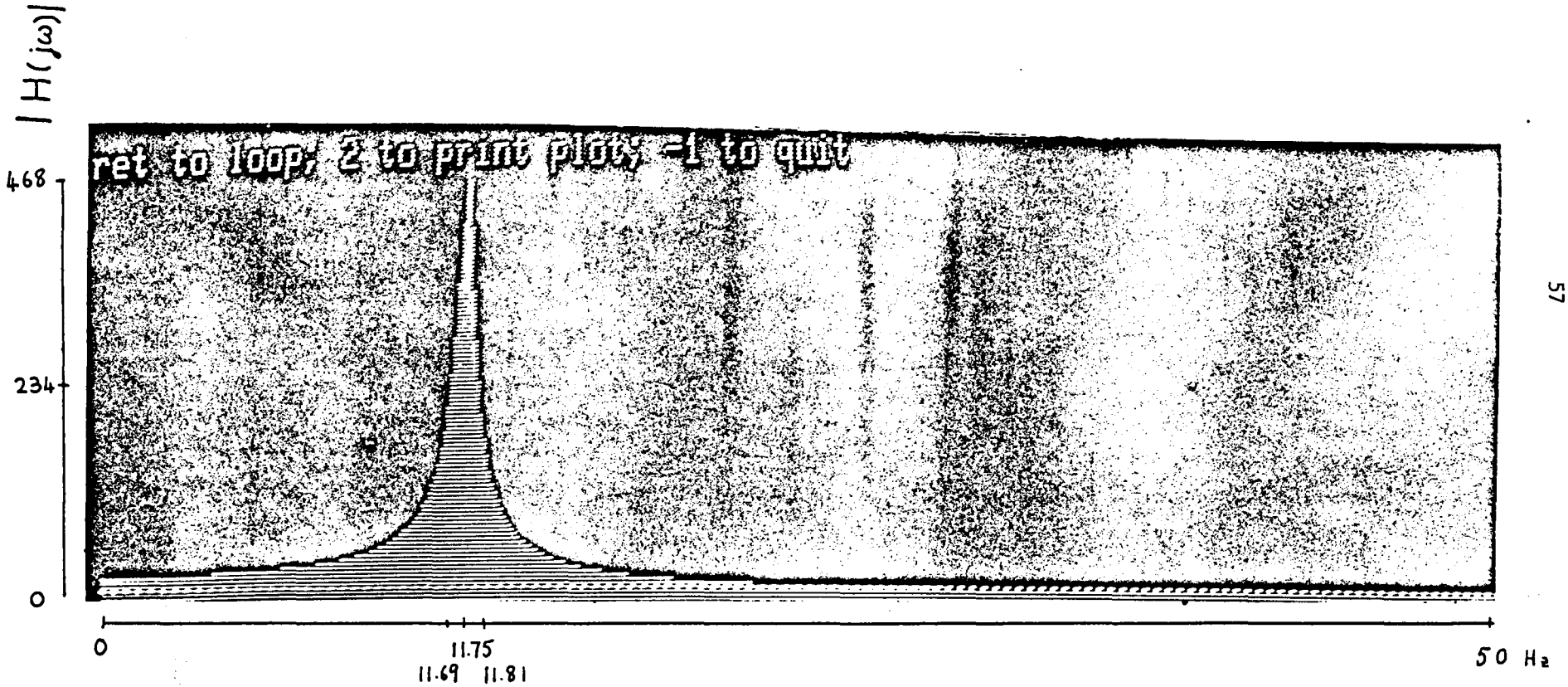

Figure 28 FFT of the analytical model of the wind on data for 0.2° pitch noise. The broadening of the peak is noticeable. (cf Fig. 27)

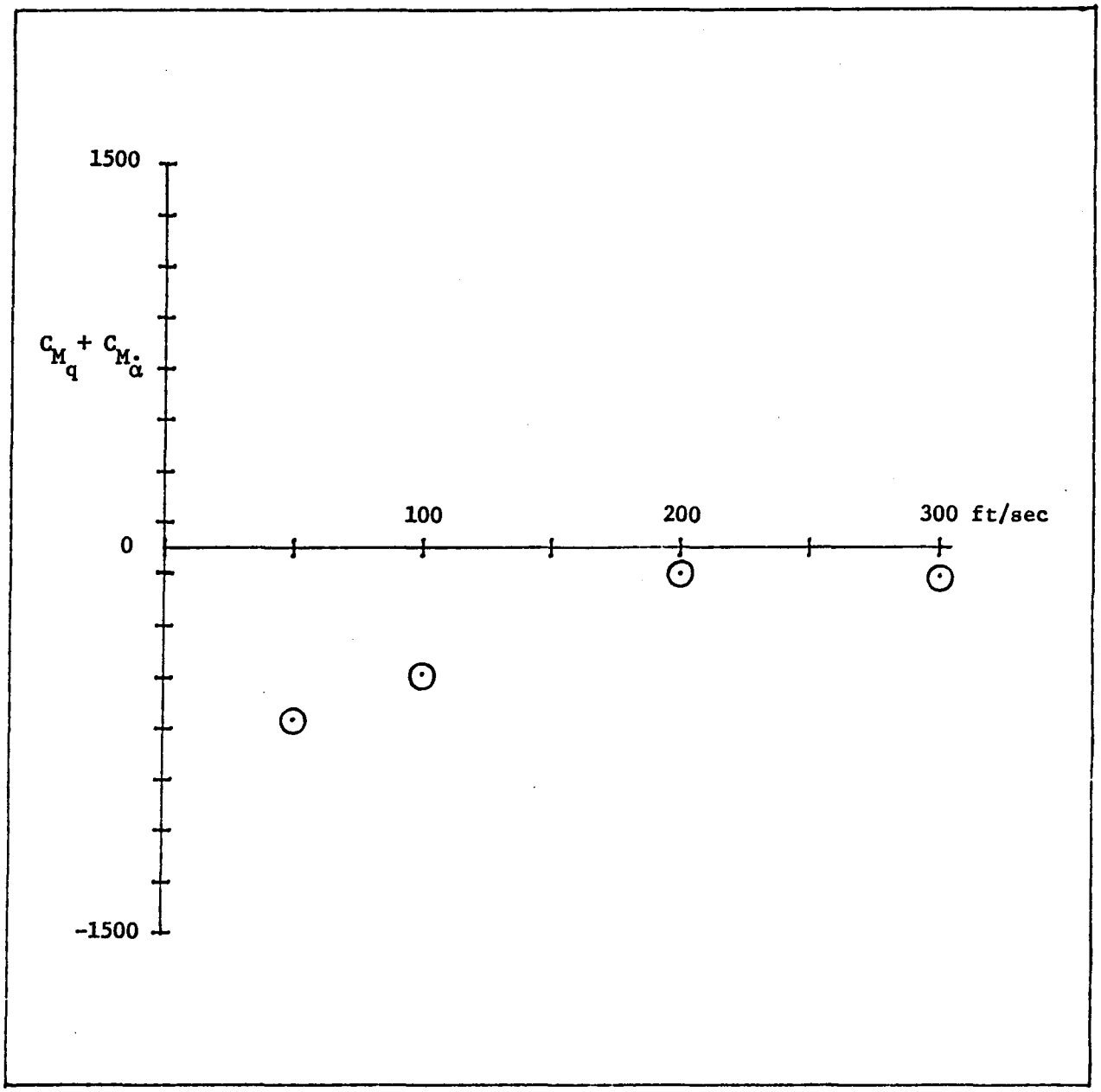

Figure 29 Pitch damping vs velocity for iron model at 2 degrees incidence

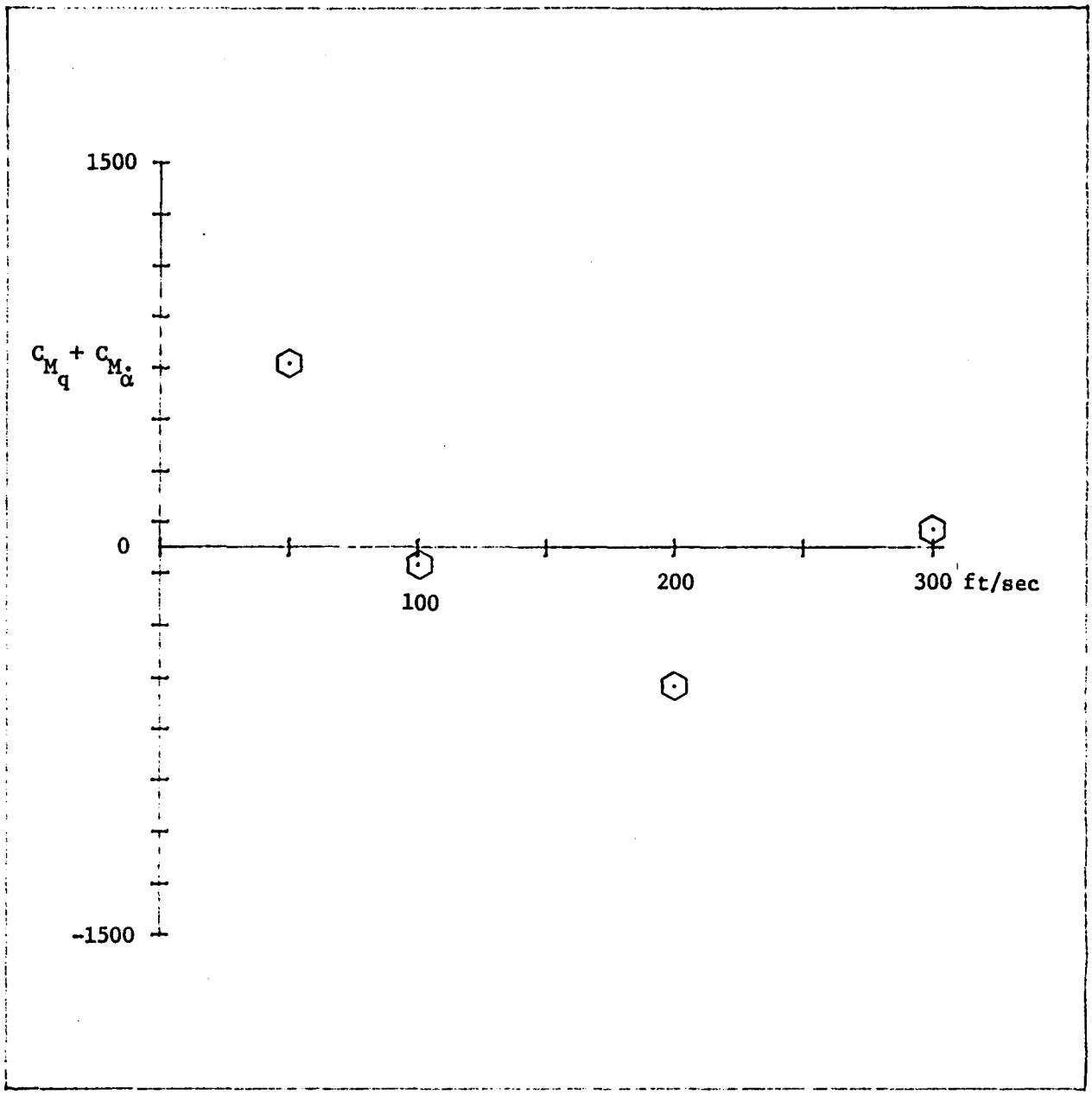

Figure 30 Pitch damping vs velocity for iron model at 4 degrees incidence

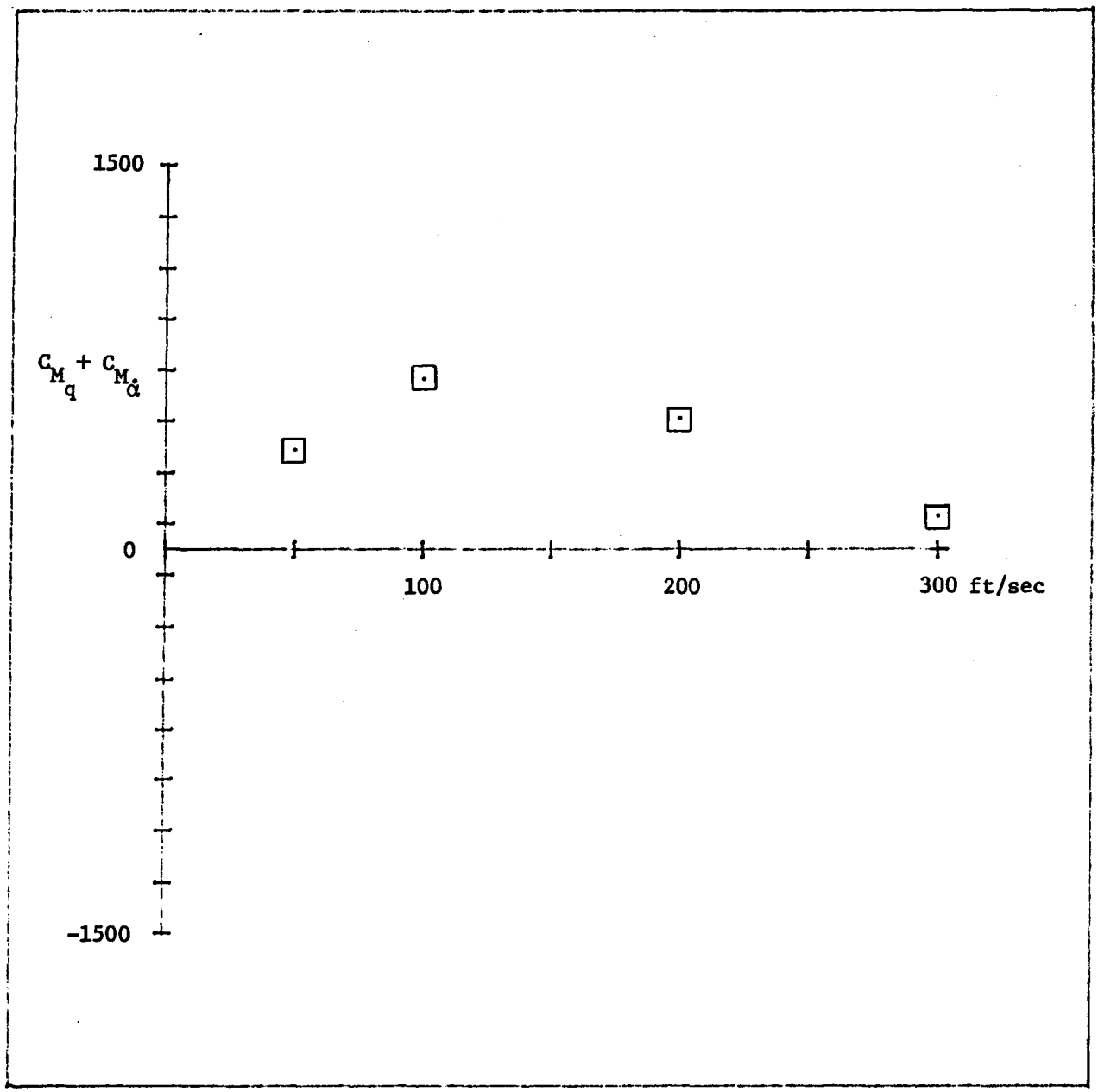

Figure 31 Pitch damping vs velocity for iron model at 8 degrees incidence

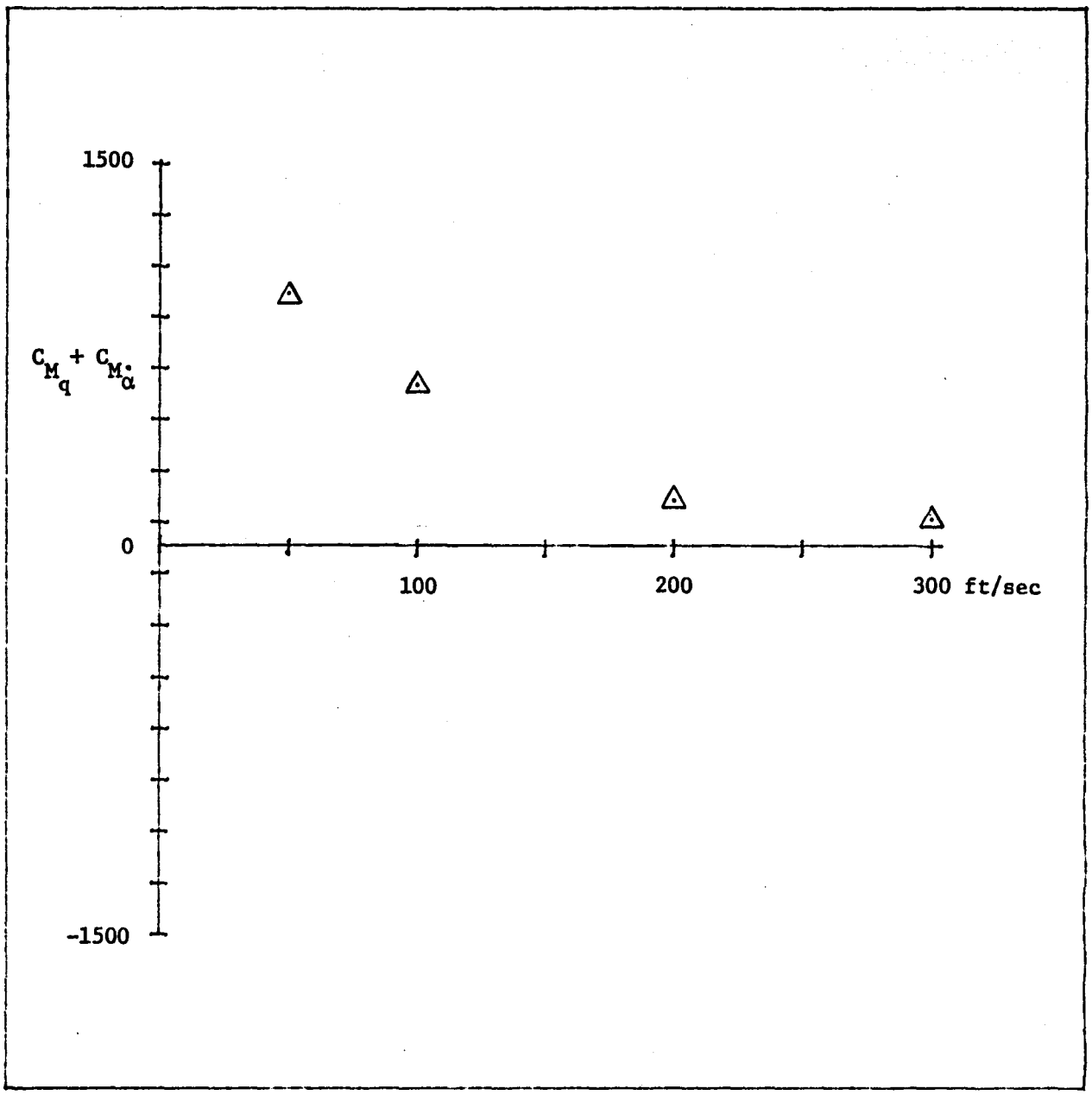

Figure 32 Pitch damping vs velocity for iron model at 16 degrees incidence

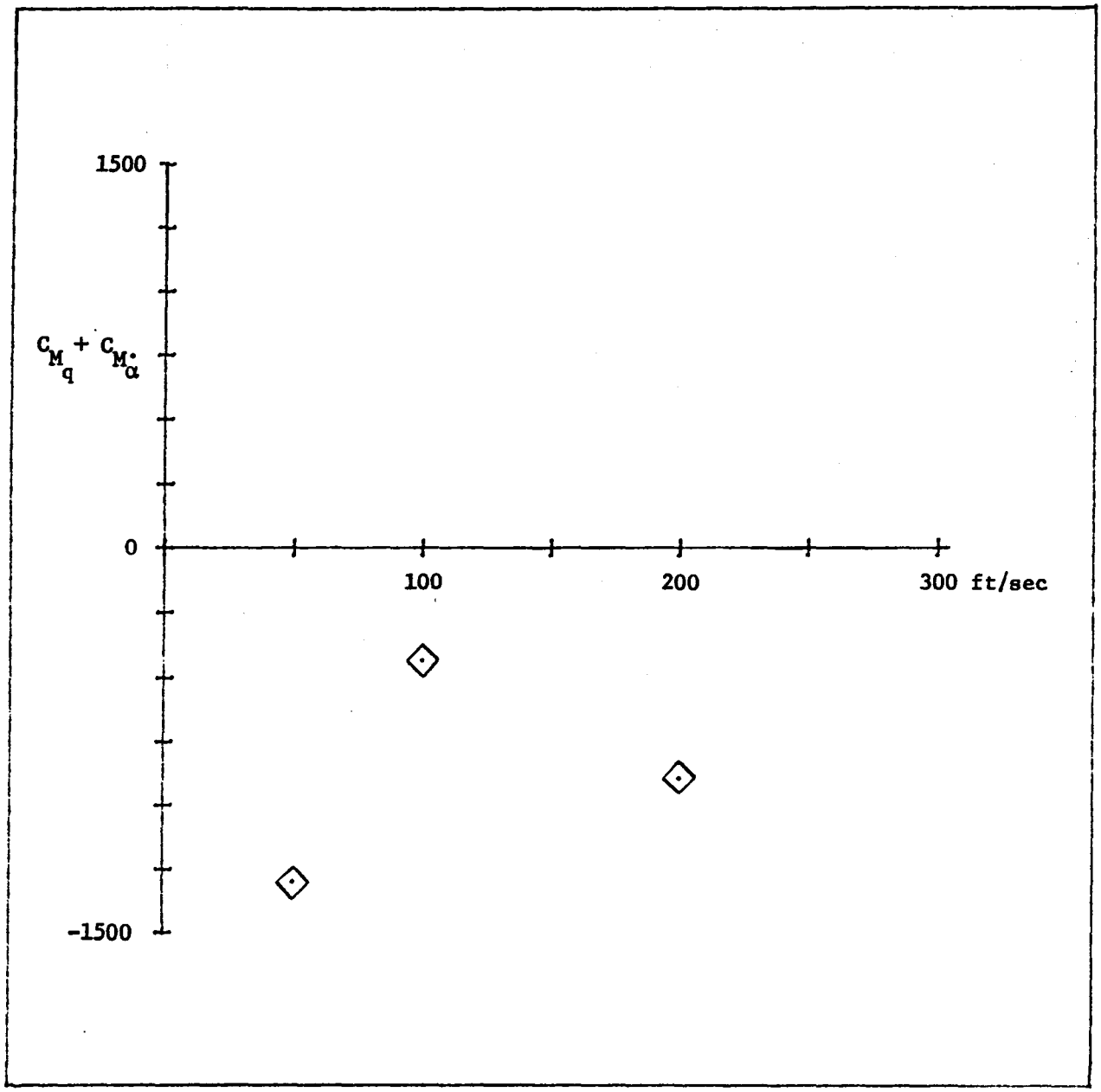

Figure 33 Pitch damping vs velocity for iron model at 32 degrees incidence

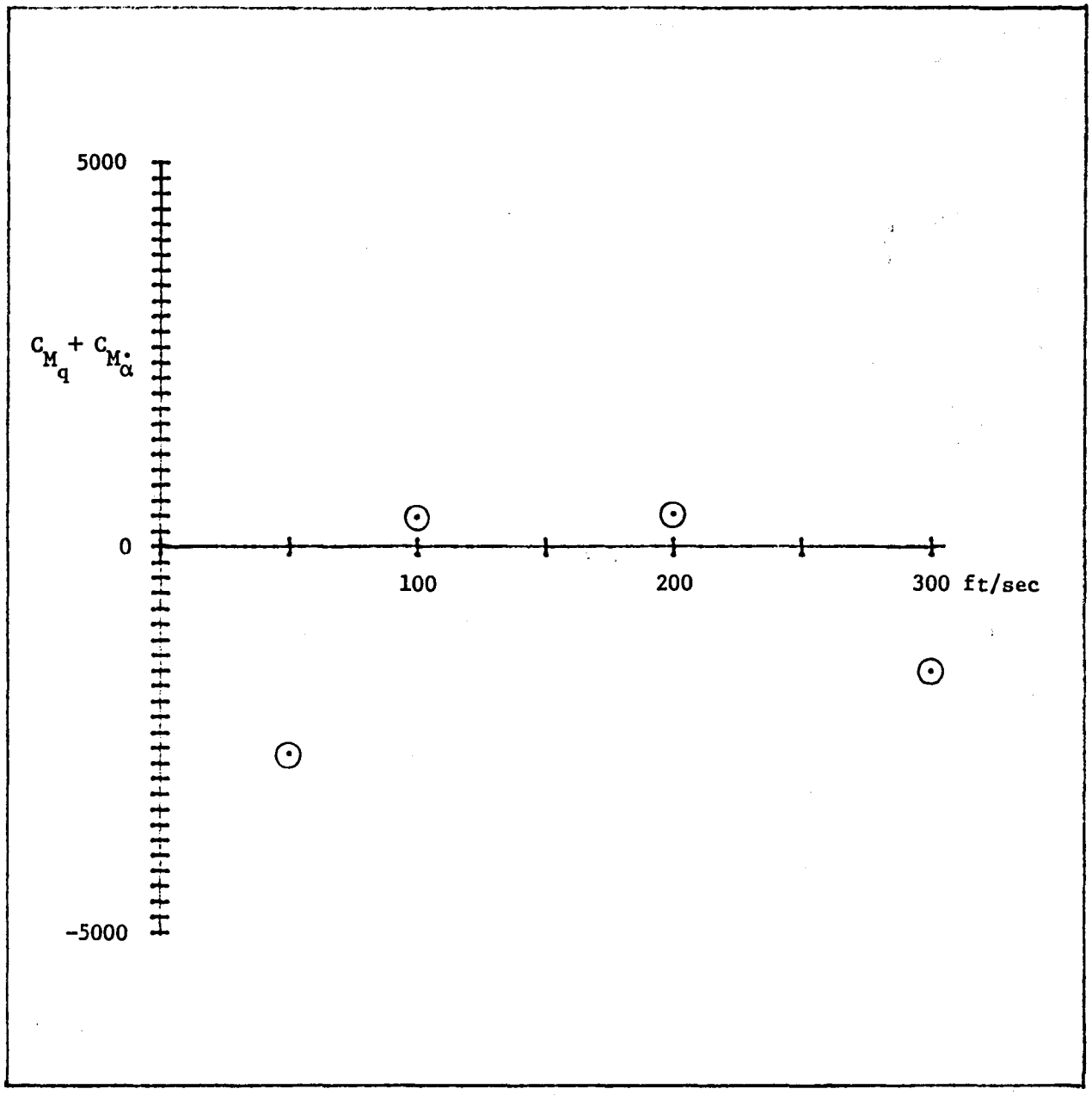

Figure 34 Pitch damping vs velocity for samarium cobalt model at 2 degrees incidence

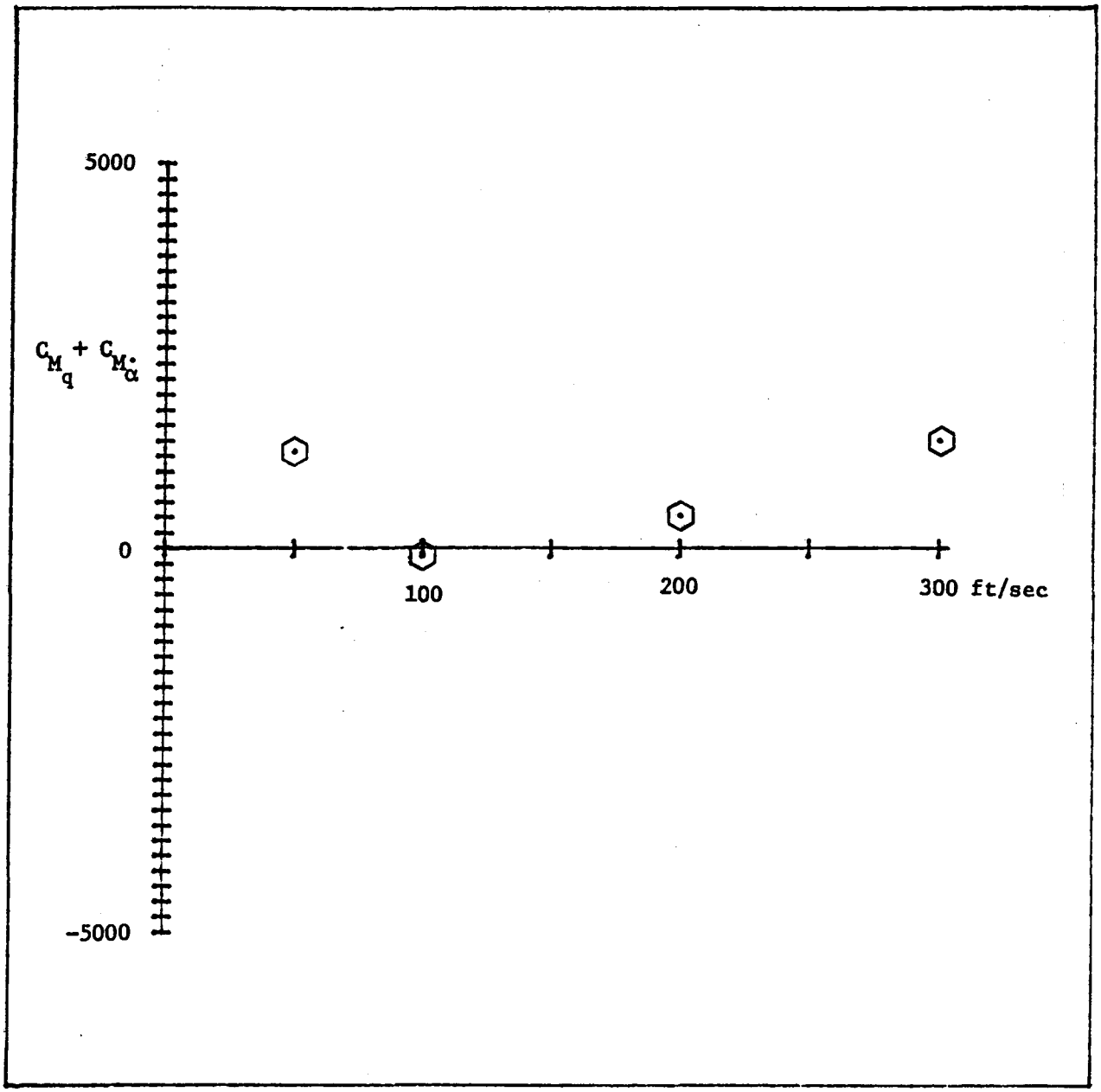

Figure 35 Pitch damping vs velocity for samarium cobalt model at 4 degrees incidence

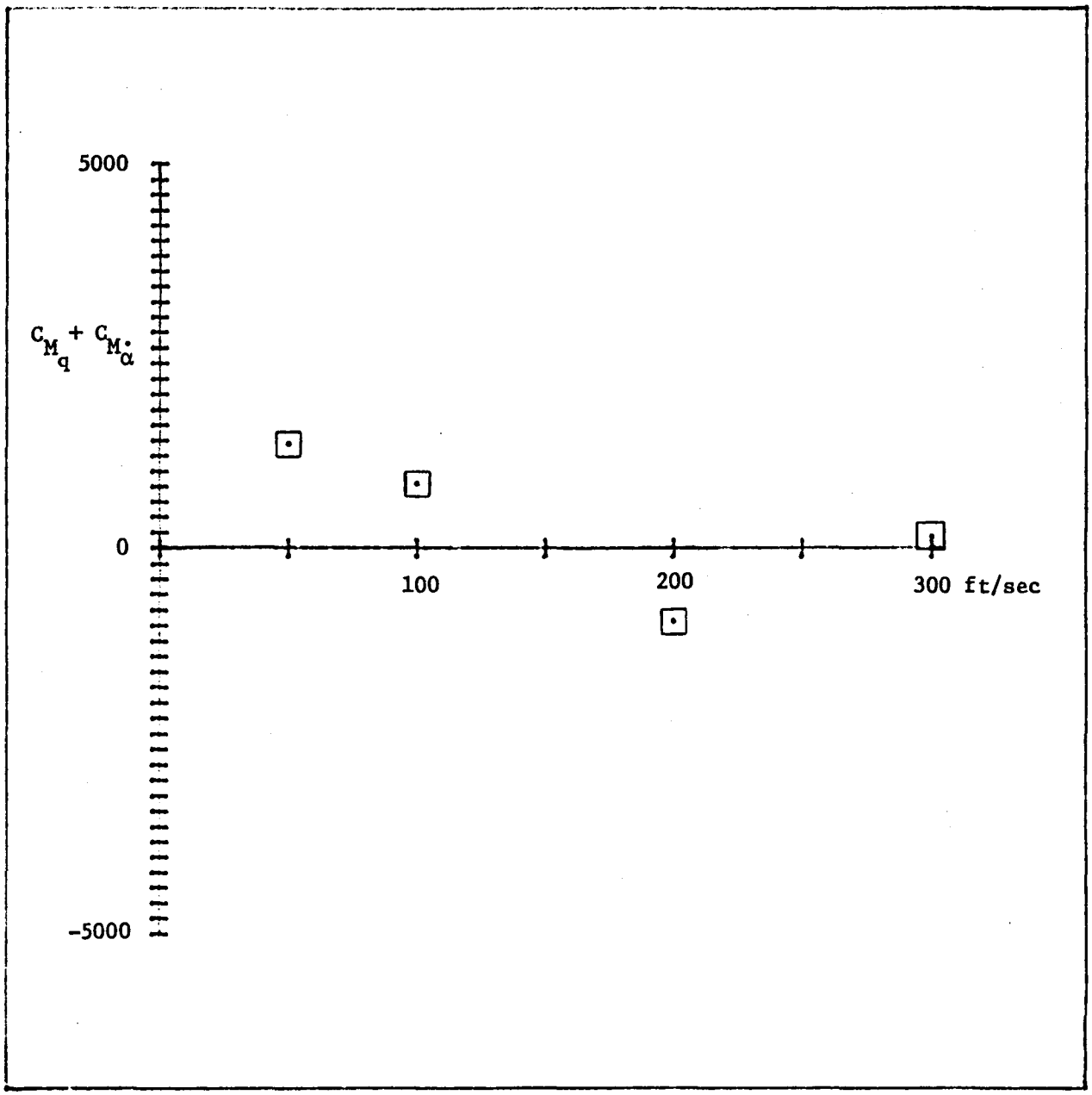

Figure 36 Pitch damping vs velocity for samarium cobalt model at 8 degrees incidence

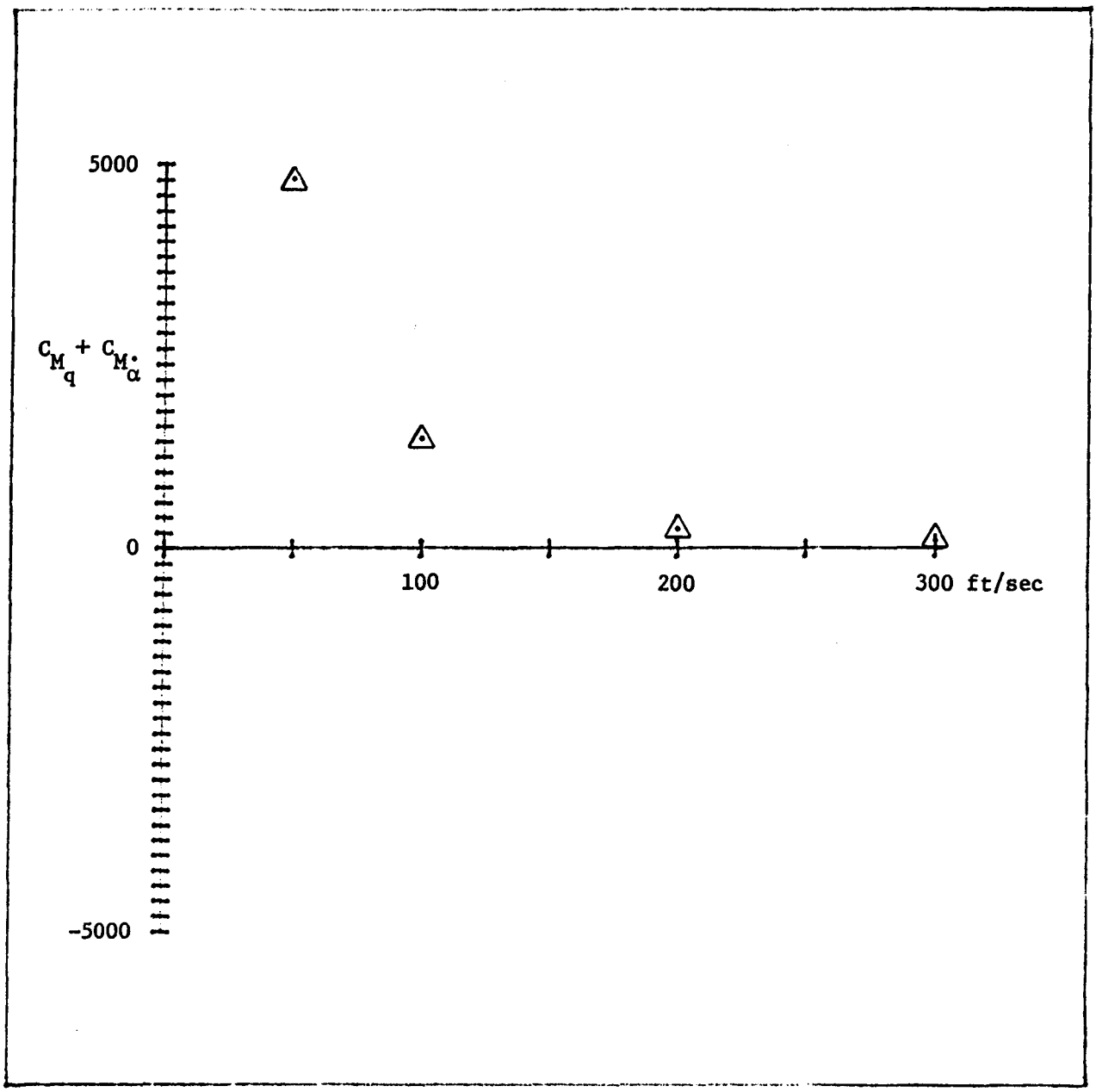

Figure 37 Pitch damping vs velocity for samarium cobalt model at 16 degrees incidence

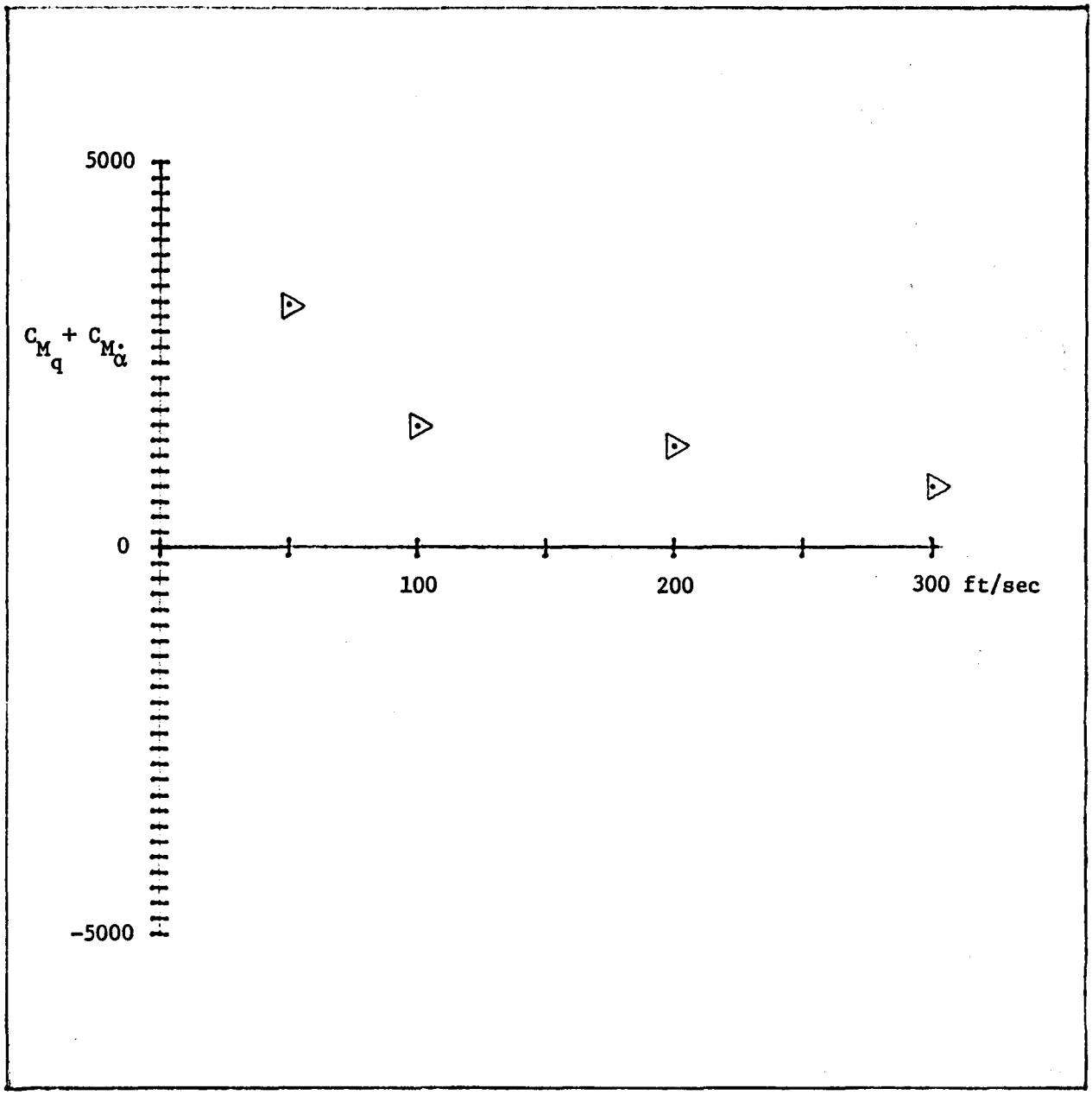

Figure 38 Pitch damping vs velocity for samarium cobalt model at 20 degrees incidence

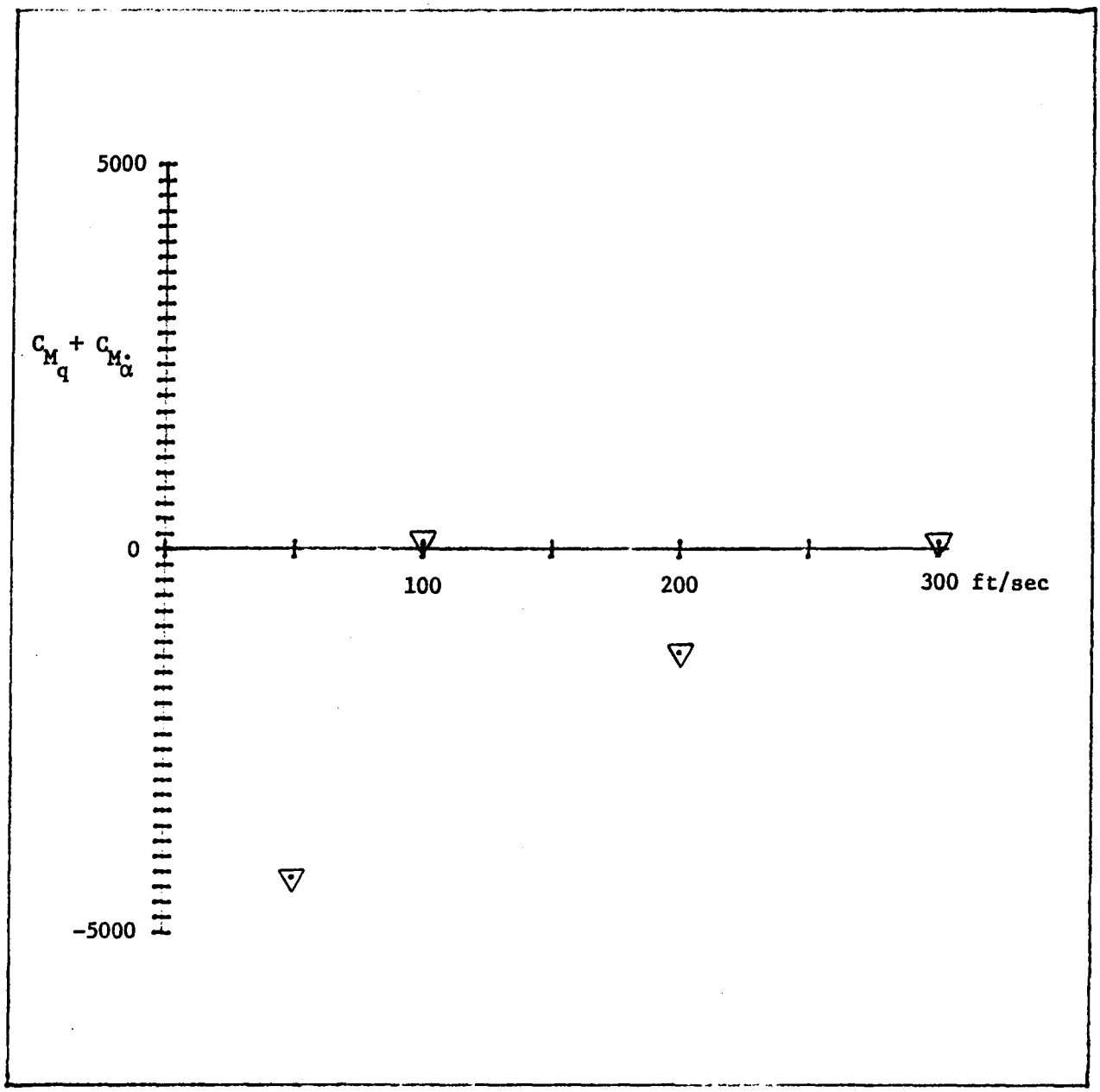

Figure 39 Pitch damping vs velocity for samarium cobalt model at 24 degrees incidence

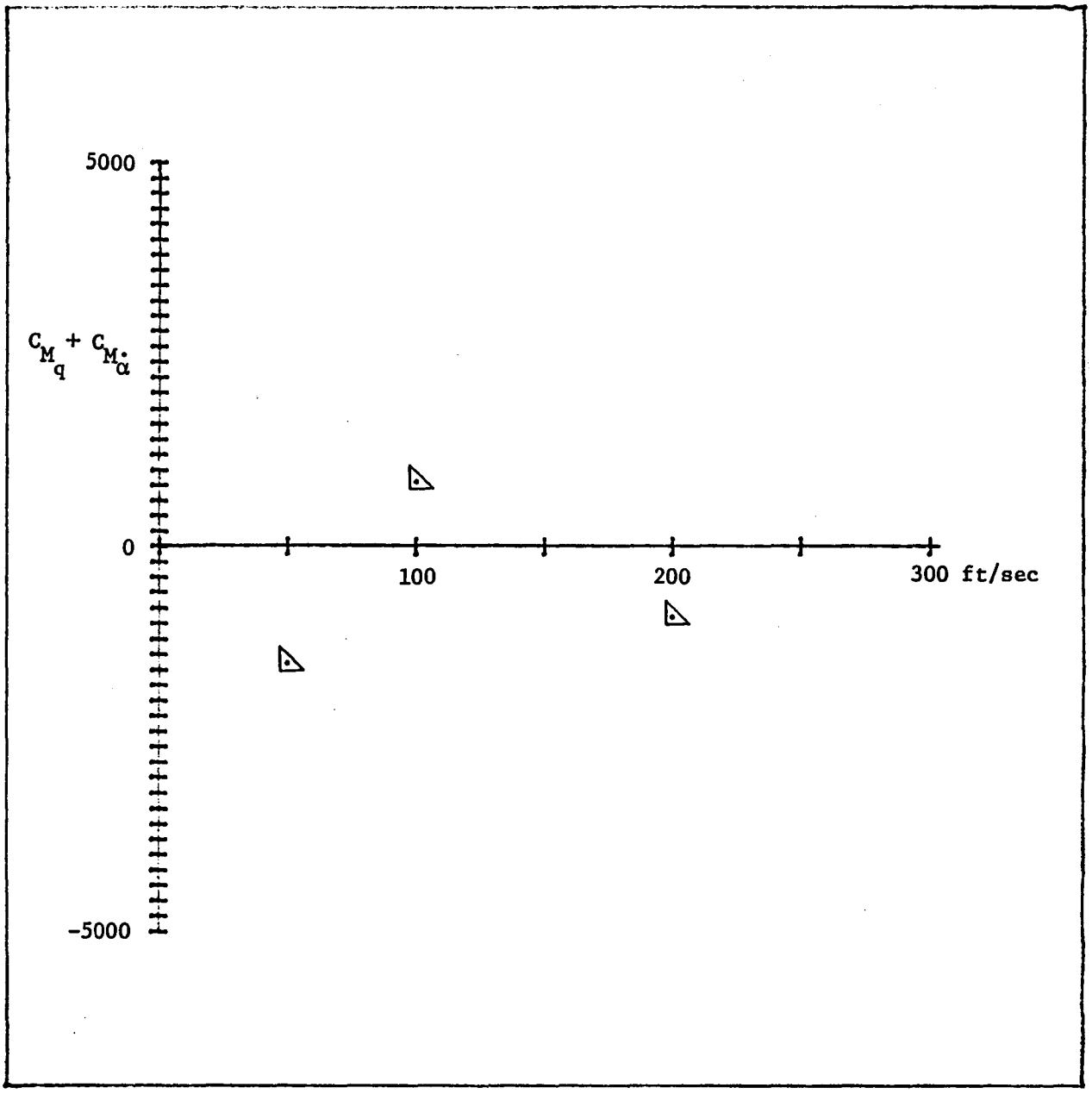

Figure 40 Pitch damping vs velocity for samarium cobalt model at 28 degrees incidence

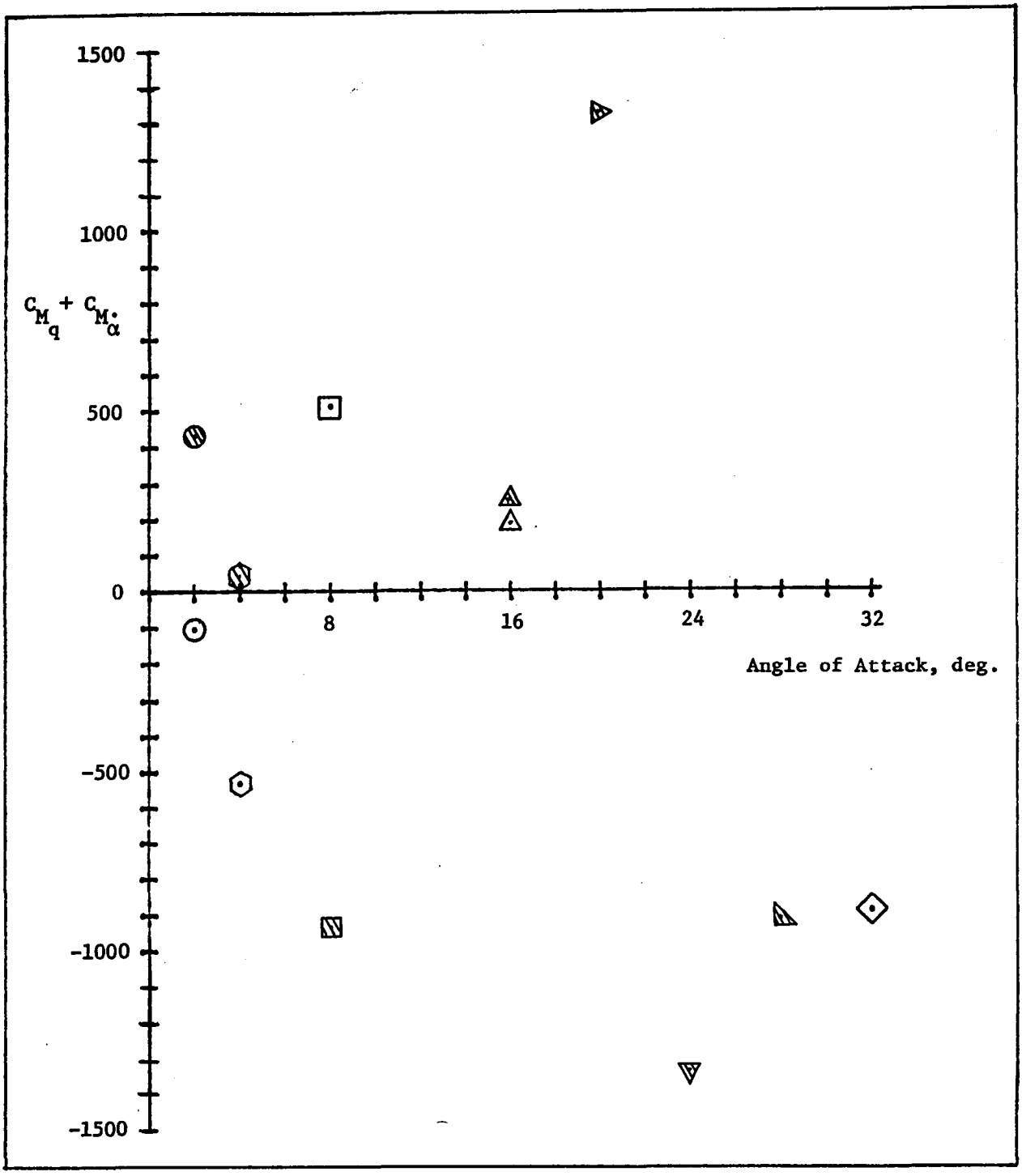

Figure 41 Pitch damping vs angle of attack for samarium cobalt model (hatched) and iron model (open) at 200 fps

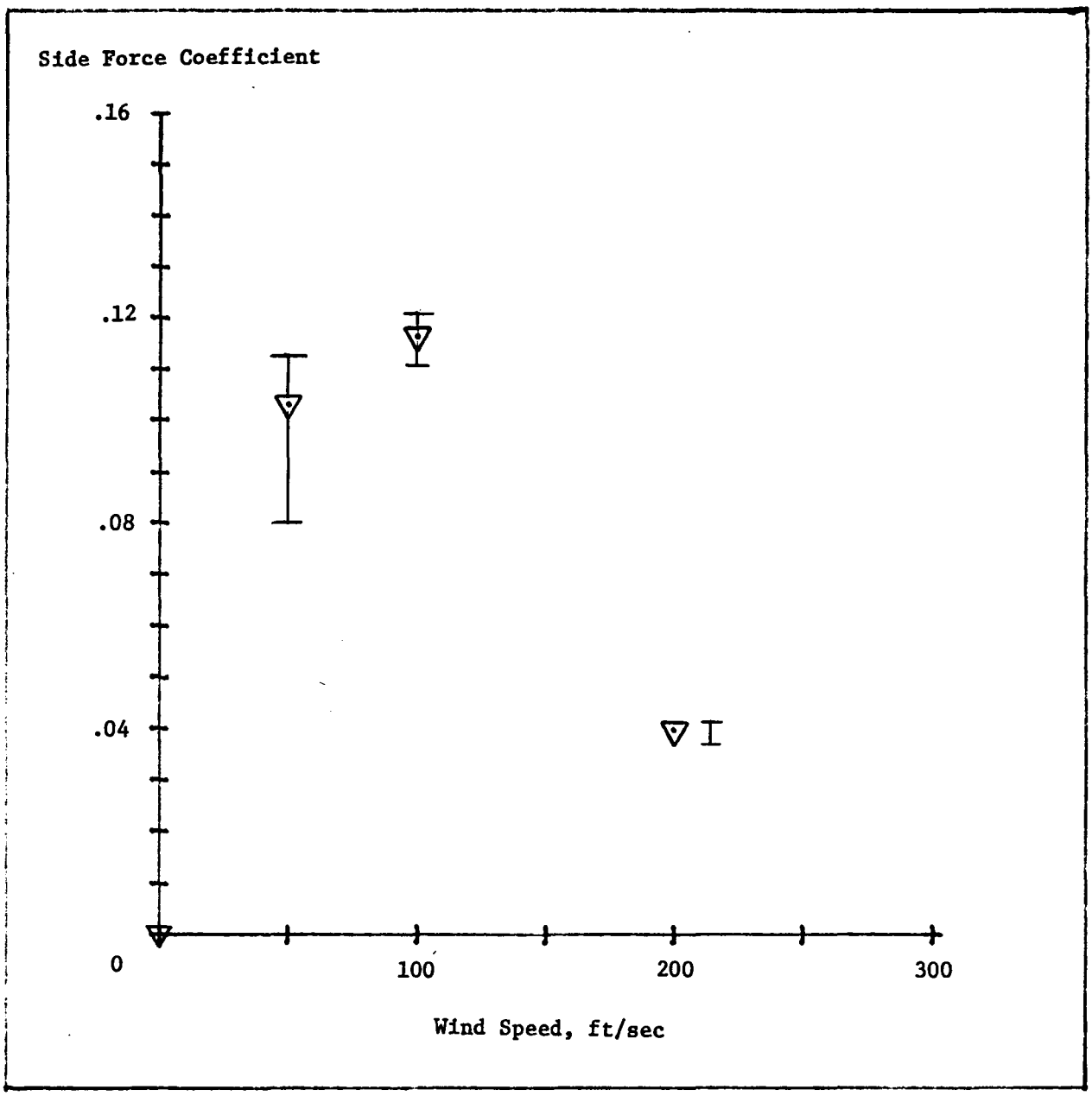

Angle of attack = 30 degrees, angle of yaw ≃ 0 degrees.

Figure 42 Side Force Coefficient vs Wind Speed

Appendix A

ESTIMATION OF MOTION-INDUCED CHANGE IN COUPLING BETWEEN A MODEL AND A PARTICULAR EPS COIL

1. It is well known that the induced EMF in a pick-up coil may be deduced from the integral

$$e = \int_A \frac{\partial \vec{\beta}}{\partial t} \cdot \vec{n} dA$$

Hence it is sufficient for these purposes to compute the normal component of the field as it is effected by the model and core geometry. Note: We assume the magnetization is instantaneous; i.e., $\frac{\partial \vec{\beta}}{\partial \tau} = \vec{f}(\text{geometry}) \frac{\partial i}{\partial t}$. However, a lag may exist. This lag is of the order of a few seconds, which is very long compared to the time required to establish the "magnetizing current". The 20 KHz field may thus never reach the shape of the D.C. field.

2. The calculations will be carried out in the following way:
   a. The magnetic potential for a sphere will be found to within an arbitrary multiplying factor that represents the uniform 20 KHz exciting field.
   b. The magnetic potential will be expressed in a cylindrical coordinate system so the pick-up coils consist of four elements: two elements at constant radius (r) and constant (x), different x's; and two at constant (r) and constant angle (ϕ).

c. The radial component of this field will be computed and integrated over the area of the coil.

d. When the model is inclined at some angle θ, the second potential is needed to describe magnetization due to the field in the normal direction; i.e.,

$$\vec{H}=Hx\left[\left(\frac{\cos^2\theta}{D_A}+\frac{\sin^2\theta}{D_C}\right)\hat{i}+\left(\sin\theta\cos\theta\right)\left(\frac{1}{D_A}-\frac{1}{D_C}\right)\hat{k}\right]$$

Thus we allow for the eccentricity of the model in computing $\vec{H}$ even though we have assumed a model so small the induced magnetic potential is essentially that due to a sphere. A similar statement can be made for a general ellipse.

The exact solution for the induced magnetic potential by an axially symmetric ellipse is known. The expansion of that potential in spherical coordinates is given in Appendix B. The result is given below in Paragraph 4.

3. A sphere of radius a centered at the origin, with permeability μ*in a uniform field F_x, has a magnetic potential

$$\Psi_x = F_x\left(x - \frac{\mu-1}{\mu+2}\cdot\frac{a^3x}{(x^2+r^2)^{3/2}}\right)$$

in the x,rΦ coordinate system. If $z = r\sin\Phi$,

$$\Psi_z = F_z\left(r\sin\Phi - \frac{\mu-1}{\mu+2}\frac{a^3 r\sin\Phi}{(x^2+r^2)^{3/2}}\right)$$

In use the uniform field part must be subtracted from Ψ_z for the cross potential. Here we define

---

*Note, the case of a perfectly conducting sphere (or approximately when the sphere is copper plated several skin depths thick) can be found by setting $\mu = 0$.

$$F_x \approx H_x / D_A \text{ and } F_z = H_x \sin\Theta\cos\Theta \left(\frac{1}{D_A} - \frac{1}{D_C}\right)$$
$$\sim M_x \qquad\qquad \approx M_z$$

Since we are interested in the effects of radial motion, two alternative procedures present themselves. In the first we offset the center of the magnetized body from 0,0 to Δr, Φ_o. The distance in the denominator of the magnetic potential thus becomes

$$x^2 + r^2 + \Delta r^2 - 2r\Delta r \cos(\Phi - \Phi_o)$$

and the derivative of this term,

$$\frac{\partial}{\partial r}\left(\frac{1}{x^2+r^2+\Delta r^2-2r\Delta r\cos(\Phi-\Phi_o)}\right) = \frac{2(r-\Delta r\cos(\Phi-\Phi_o))}{(x^2+r^2+(\Delta r)^2-2r\Delta r\cos(\Phi-\Phi_o))^2}$$

The second procedure is to change the position of the coil and is much more complicated.

If the model were to have a yaw angle, ϕ, the perturbation field in yaw becomes

$$\partial\delta\Psi_y \approx M_y \left(-\frac{\mu-1}{\mu+2}\frac{a^2\, r\cos\phi}{(x^2+r^2)^{3/2}}\right)$$

Here M_y is the magnetization in the yaw direction if it exists.

Note: $\vec{H} = -\nabla\Psi$.

4. In ellipsoidal coordinates u,v,Φ, one finds

$$\Psi = F \left\{ \cosh u \cos v + \frac{\frac{a}{c}\left(\left(\frac{a}{c}\right)^2 - 1\right)(\mu - 1)\cos v}{1-(\mu-1)\frac{b^2}{c^2}\left(1 + \frac{a}{2c}\ell n \frac{a-c}{a+c}\right)} \right.$$

$$\left. \left(1 + \cosh \frac{u}{2} \ell n \frac{\cosh u-}{\cosh u+}\right) \right\}$$

where a = semimajor axis (in x direction)
b = semiminor axis
$c = \sqrt{a^2 - b^2}$

$a = c \cosh u_o$, $b = c \sinh u_o$

$x = c \cosh u \cos v$

$r = c \sinh u \sin v$

$\Phi = i \left(\tan^{-1} \frac{z}{y}\right)$

If this is expanded into a form compatible with spherical coordinates in powers of (c/a) ($c \to 0$ for a sphere) one obtains

$$\Psi \simeq F_x (x)$$

5. The coils of the EPS which are of interest can be described by two straight lines and arcs of two circles. Thus we are interested in the area integral

$$I = \int_{\Phi_1}^{\Phi_2} \int_{x_1}^{x_2} M (x,R,\Phi)\, dx\, Rd\Phi$$

Here R is the radius of the cylinder of the coil axis.

6. With all this background we can now compute the radial component of the field

$$H_r = -\frac{\partial \Psi}{\partial r}$$

$$H_r = H_x \left\{ 3 \frac{\mu-1}{\mu+2} a^3 x \cdot \frac{(r - \Delta r \cos(\Phi-\Phi_o))}{(x^2+r^2+(\Delta r)^2-2r\Delta r\cos(\Phi-\Phi_o))^{5/2}} \right\}$$

$$+ H_x \sin\Theta \cos\Theta \frac{\mu-1}{\mu+2} a^3 \left(1 - \frac{D_A}{D_C}\right) \cdot$$

$$\left\{ \frac{(r-\Delta r\cos(\Phi-\Phi_o))\sin\Phi - 3(r^2+(\Delta r)^2-2r\Delta r\cos(\Phi-\Phi_o))^2 (r-\Delta r\cos(\Phi-\Phi_o))\sin\Phi}{\sqrt{r^2+(\Delta r)^2-2r\Delta r\cos(\Phi-\Phi_o)}\,(x^2+r^2+(\Delta r)^2-2r\Delta r\cos(\Phi-\Phi_o))^{3/2} r (x^2+r^2-2r\Delta r\cos(\Phi-\Phi_o))^{5/2}} \right\}$$

Note,

$$\frac{1}{(x^2+r^2+\Delta r^2-2r\Delta r\cos(\Phi-\Phi_o))^{n/2}} \simeq \frac{1}{(x^2+r^2)^{n/2}} \left(1 + \frac{nr\Delta r}{x^2+r^2} \cos(\Phi-\Phi_o)+\ldots\right.$$

This latter approximation neglects terms

$$0 \left(\frac{(\Delta r)^2}{x^2+r^2}\right.$$

7. Making the linearized assumptions

$$M_r \simeq M_x \cdot a^3 \frac{\mu-1}{\mu+2}\left\{\frac{3xr}{(x^2+r^2)^{5/2}}\left(1+\left(1-\frac{5r^2}{x^2+r^2}\right)\frac{\Delta r}{r}\cos(\Phi-\Phi_o)\right)\right.$$

$$+ \sin\Theta\cos\Theta\left(1-\frac{D_A}{D_C}\right)\sin\Phi\left(\frac{1+\frac{3r^2}{x^2+r^2}\cdot\frac{\Delta r}{r}\cos(\Phi-\Phi_o)}{(x^2+r^2)^{3/2}}\right.$$

$$\left.\left.-\frac{3r^2\left(1-5\left(1-\frac{r^2}{x^2+r^2}\right)\right)\frac{\Delta r}{r}\cos(\Phi-\Phi_o)}{(x^2+r^2)^{5/2}}\right\}\right.$$

8. Comparing Paragraphs 5 and 7 we see there are eight integrals involved in approximating e in Paragraph 1.

$$I_1 = R^2\int_{\Phi_1}^{\Phi_2}\int_{x_1}^{x_2}\frac{3x\,dx\,d\Phi}{(x^2+R^2)^{5/2}};\quad I_2 = R^2\int_{\Phi_1}^{\Phi_2}\int_{x_1}^{x_2}\frac{3x\cos(\Phi-\Phi_o)\,dx\,d\Phi}{(x^2+R^2)^{5/2}}$$

$$I_3 = R^4\int_{\Phi_1}^{\Phi_2}\int_{x_1}^{x_2}\frac{15x\cos(\Phi-\Phi_o)\,dx\,d\Phi}{(x^2+R^2)^{7/2}};\quad I_4 = R\int_{\Phi_1}^{\Phi_2}\int_{x_1}^{x_2}\frac{dx\,d\Phi\,\sin\Phi}{(x^2+R^2)^{3/2}}$$

$$I_5 = R^3\int_{\Phi_1}^{\Phi_2}\int_{x_1}^{x_2}\frac{3\cos(\Phi-\Phi_o)\,dx\,d\Phi\,\sin\Phi}{(x^2+R^2)^{5/2}};\quad I_6 = R^3\int_{\Phi_1}^{\Phi_2}\int_{x_1}^{x_2}\frac{3\,dx\,d\Phi\,\sin\Phi}{(x^2+R^2)^{5/2}}$$

$$I_7 = R^3 \int_{\Phi_1}^{\Phi_2} \int_{x_1}^{x_2} \frac{15 \cos(\Phi-\Phi_o)dx\, d\Phi \sin \Phi}{(x^2+R^2)^{5/2}} = 5I_5;$$

$$I_8 = R^5 \int_{\Phi_1}^{\Phi_2} \int^{x_2} \frac{15 \cos(\Phi-\Phi_o)dx\, d\Phi \sin \Phi}{(x^2+R^2)^{7/2}}$$

9. Thus,

$$e \simeq M_x \cdot a^3 \frac{\mu-1}{\mu+2} \left\{ I_1 + (I_2-I_3)\frac{\Delta r}{R} + \sin\Theta\cos\Theta\left(1 - \frac{D_A}{D_C}\right)(I_4-I_6+(6I_5-I_8)\frac{\Delta r}{R}) \right\}$$

This relation is of great value because it allows us to estimate the performance of a given coil in response to motion of the magnetized model.

I. Centered model

$$e_o \simeq M_x \cdot a^3 \frac{\mu-1}{\mu+2} R^2 (\Phi_2-\Phi_1) \left(\frac{1}{(x_1^2 + R^2)^{3/2}} - \frac{1}{(x_2^2 + R^2)^{3/2}} \right.$$

e_o is the reference value. It may vary from coil to coil, depending upon how well R, Φ, x are known. Note e_o is proportional to the volume of the model and the area of the coil. Note, too, the perturbation field decays like the reciprocal of distance cubed, which is quite rapid.

II. Model perturbed a distance Δx, angle of attack zero

$$e_{\Delta x} = e_o - M_x a^3 \frac{\mu-1}{\mu+2} R^2 (\Phi_2-\Phi_1) \left(\frac{3x_1 R}{(x_1^2 + R^2)^{5/2}} - \frac{3x_2 R}{(x_2^2 + R^2)^{5/2}} \right. \frac{\Delta x}{R}$$

III. Model perturbed in radial direction, $\Delta x=0$, angle of attack zero. If $\Phi_o = (o,\pi)$, this is y displacement, if $\Phi_o=(\frac{\pi}{2}, \frac{3\pi}{2})$, it is vertical

$$e_{\Delta r \Phi_o} = e_o - M_x a^3 \frac{\mu-1}{\mu+2} R^2(\sin(\Phi_2-\Phi_o)-\sin(\Phi_1-\Phi_o))(g_2-g_3) \frac{\Delta r}{R}$$

where $$g_2-g_3 = \frac{R^3}{(x_1^2+R^2)^{3/2}} - \frac{R^3}{(x_2^2+R^2)^{3/2}} - \frac{R^5}{(x_1^2+R^2)^{5/2}} + \frac{R^5}{(x_2^2+R^2)^{5/2}}$$

IV. Model pitched an angle Θ, $\Delta x=0$, $\Delta r=0$

$$e \simeq e_o + M_x a^3 \frac{\mu-1}{\mu+2} \cdot R^2 \sin\Theta\cos\Theta\left(1-\frac{D_A}{D_C}\right)(\sin\Phi_2-\sin\Phi_1)(g_4-g_6)$$

where $$g_4-g_6=\left(1-\frac{R^2}{3R^2}\right)\left(\frac{x_2}{\sqrt{x_2^2+R^2}} - \frac{x_1}{\sqrt{x_1^2+R^2}} + \frac{R^2 x_1\sqrt{x_1^2+R^2}}{3(x_1^2+R^2)^2} - \frac{R^2 x_2\sqrt{x_2^2+R^2}}{3(x_1^2+R^2)^2}\right.$$

The term in Θ is due to the rotation of the magnetization vector. Hence, there is a similar term in angle of yaw when $\Theta = 0$. This constitutes the complete collection of linear terms.

10. Cross coupling terms abound. Clearly from Paragraph 7 one can see Δx, Δr, $\Delta\Phi$ products. There is a suppressed coefficient of the 3xr, etc. term, namely

$$\frac{\cos^2\Theta}{D_A} + \frac{\sin^2\Theta}{D_B}$$

which must be included if second order terms are to be accounted for. The formula in Paragraph 7 has one other implication. If $\Phi_o = \pi/2$, the perturbation is in the z direction

$$\Delta r \cos\left(\Phi - \frac{\pi}{2}\right) = \Delta z \sin \Phi$$

This means three coils are necessary to sort out Δx, Δz and θ to a first order because there are three terms that contribute to ΔM_r due to displacement. That is, the system tends to solve three simultaneous equations for each set of displacements. Note a redundancy exists in Δx! This redundancy is removed if roll is measurable because now one must solve all the equations at once; i.e., the magnetic potential may be written

$$\Psi = M_x\left(x - \frac{\mu-1}{\mu+2} \cdot \frac{a^3 x}{(x^2+r^2+(\Delta r)^2 - 2r\Delta r\cos(\Phi-\Phi_o))^{3/2}}\right.$$

$$- M_y \frac{\mu-1}{\mu+2}\left(\frac{a^3\sqrt{r^2+(\Delta r)^2-2r\Delta r\cos(\Phi-\Phi_o)}\cos\Phi}{(x^2+r^2+(\Delta r)^2-2r\Delta r\cos(\Phi-\Phi_o))^{3/2}}\right)$$

$$\left. - M_z \frac{\mu-1}{\mu+2}\left(\frac{a^3\sqrt{r^2+(\Delta r)^2-2r\Delta r\cos(\Phi-\Phi_o)}\sin\Phi}{(x^2+r^2+(\Delta r)^2-2r\Delta r\cos(\Phi-\Phi_o))^{3/2}}\right)\right)$$

Now, M_x, M_y, M_z are functions of pitch, yaw and roll angle through the usual transformations. This implies three contributions. The x, Δr, Φ_o implies three additional contributions. Hence, six coils are needed.

In the past the sensitivity was doubled by adding or subtracting opposed coils in easily defined ways. Thus, the number of coils becomes six for plane motion and only twelve for complete motion!

Appendix B

Table of Integrals

$$I_1 = R^2 \int_{\Phi_1}^{\Phi_2} \int_{x_1}^{x_2} \frac{3x\, dx\, d\Phi}{(x^2+R^2)^{5/2}} = R^2(\Phi_2-\Phi_1) \cdot \frac{3}{2} \int_{x_1}^{x_2} \frac{2x\, dx}{(x^2+R^2)^{5/2}}$$

$$I_1 = R^2(\Phi_2-\Phi_1) \left(\frac{1}{(x_1^2+R^2)^{3/2}} - \frac{1}{(x_2^2+R^2)^{3/2}}\right)$$

$$I_2 = R^2 \int_{\Phi_1}^{\Phi_2} \int_{x_1}^{x_2} \frac{3x\cos(\Phi-\Phi_o)\, dx d\Phi}{(x^2+R^2)^{5/2}} = R^2(\sin(\Phi_2-\Phi_o)-\sin(\Phi_1-\Phi_o)) \left(\frac{1}{(x_1^2+R^2)^{3/2}} - \frac{1}{(x_2^2+R^2)^{3/2}}\right)$$

$$I_3 = R^4 \int_{\Phi_1}^{\Phi_2} \int_{x_1}^{x_2} \frac{15x\cos(\Phi-\Phi_o)\, dx d\Phi}{(x^2+R^2)^{7/2}} = 3R^4(\sin(\Phi_2-\Phi_o)-\sin(\Phi_1-\Phi_o)) \left(\frac{1}{(x_1^2+R^2)^{5/2}} - \frac{1}{(x_2^2+R^2)^{5/2}}\right)$$

$$I_4 = R \int_{\Phi_1}^{\Phi_2} \int_{x_1}^{x_2} \frac{\sin\Phi\, dx\, d\Phi\, dx}{(x^2+R^2)^{3/2}} = R(\sin\Phi_2-\sin\Phi_1) \cdot \int_{x_1}^{x_2} \frac{dx}{(x^2+R^2)^{3/2}}$$

$$I_4 = R(\sin\Phi_2-\sin\Phi_1)\left\{\frac{x}{R^2}\cdot\frac{1}{\sqrt{x^2+R^2}}\right\}\Bigg|_{x_1}^{x_2} R(\sin\Phi_2-\sin\Phi_1)$$

$$\left(\frac{x_2}{R^2\sqrt{x_2^{\,2}+R^2}} - \frac{x_1}{R^2\sqrt{x_1^{\,2}+R^2}}\right)$$

All these integrals are in the form $f(y)\cdot g(x)$.

Thus, $I_4 = Rf_4(\Phi)\cdot g_4(x)$

where $f_4(\Phi) = \sin\Phi_2-\sin\Phi_1$

$$g_4(x) = \frac{x_2}{R^2\sqrt{x_2^{\,2}+R^2}} - \frac{x_1}{R^2\sqrt{x_1^{\,2}+R^2}}$$

Note $f_6=f_4$ and $f_5=f_7=f_8=\cos\Phi_o\left(\frac{-\cos^2\Phi_2+\cos^2\Phi_1}{2}\right) + \sin\Phi_o\left(\frac{\Phi_2-\Phi_1}{2}\right)$

$$- \frac{\sin\Phi_o}{4}(\sin 2\Phi_2 - \sin 2\Phi_1)$$

Note g_5, g_6, g_7 all involve $\int_{x_1}^{x_2} \frac{dx}{(x^2+R^2)^{5/2}}$. From Pierce Integral Table, page 24, #164

$$g_5 = \int_{x_1}^{x_2} \frac{dx}{(x^2+R^2)^2\sqrt{x^2+R^2}} = \frac{x\sqrt{x^2+R^2}}{3\ R^2(x^2+R^2)^2}\Bigg|_{x_1}^{x_2} + \frac{1}{3R^2}\int_{x_1}^{x_2} \frac{dx}{(x^2+R^2)\sqrt{x^2+R^2}}$$

But the second integral is clearly g_4.

Similarly,

$$g_8 = \int_{x_1}^{x_2} \frac{dx}{(x^2+R^2)^3\sqrt{x^2+R^2}} = \frac{x\sqrt{x^2+R^2}}{5\ R^2(x^2+R^2)^3}\Bigg|_{x_1}^{x_2} + \frac{2}{5R^2}\int_{x_1}^{x_2} \frac{dx}{(x^2+R^2)^2\sqrt{x^2+R^2}}$$

$$g_8 = \frac{x\sqrt{x^2+R^2}}{5R^2(x^2+R^2)^3}\Bigg|_{x_1}^{x_2} + \frac{2}{5R^2}\ g_5$$

$$g_5 = \frac{\sqrt{x^2+R^2}}{3R^2(x^2+R^2)^2}\Bigg|_{x_1}^{x_2} + \frac{1}{3R^2}\ g_4$$

$$g_4 = \frac{x_2}{R^2\sqrt{x_2^2+R^2}} - \frac{x_1}{R^2\sqrt{x_1^2+R^2}}$$

$I_5 = 3R^3\ f_5 g_5$; $\qquad I_6 = 3R^3\ f_4 g_5$

$I_7 = 15R^3\ f_5 g_5$; $\qquad I_8 = 15R^5\ f_5 g_8$

1. Report No.	2. Government Accession No.	3. Recipient's Catalog No.
NASA CR-166017		

4. Title and Subtitle	5. Report Date
Development of Closed Loop Roll Control for Magnetic Balance Systems	October 1982
	6. Performing Organization Code
7. Author(s)	8. Performing Organization Report No.
Eugene E. Covert, Charles W. Haldeman, Gautham Ramohalli, and Peter Way	
9. Performing Organization Name and Address	10. Work Unit No.
Massachusetts Institute of Technology Department of Aeronautics and Astronautics Cambridge, Massachusetts 02139	11. Contract or Grant No. NSG-1502
12. Sponsoring Agency Name and Address	13. Type of Report and Period Covered Final Report Feb. '78 to Feb. '82
National Aeronautics and Space Administration Washington, D. C. 20546	14. Sponsoring Agency Code 505-31-53-10

15. Supplementary Notes

Langley Technical Monitor: Richmond P. Boyden

16. Abstract

This research was undertaken with the goal of demonstrating closed loop control of the roll degree of freedom on the NASA prototype magnetic suspension and balance system at the MIT Aerophysics Laboratory, thus, showing feasibility for a roll control system for any large magnetic balance system which might be built in the future. During the research under this grant, study was directed toward the several areas of torque generation, position sensing, model construction and control system design. These effects were then integrated to produce successful closed loop operation of the analogue roll control system. This experience indicated the desirability of microprocessor control for the angular degrees of freedom.

17. Key Words (Suggested by Author(s))	18. Distribution Statement
Magnetic suspension Magnetic balance Roll control	Unclassified - Unlimited Star Category - 09

19. Security Classif. (of this report)	20. Security Classif. (of this page)	21. No. of Pages	22. Price
Unclassified	Unclassified	87	A05

End of Document